Implementation of Warm-Cloud Processes in a Source-Oriented WRF/Chem Model to Study the Effect of Aerosol Mixing State on Fog Formation in the Central Valley of California

Hsiang-He Lee[1*], Shu-Hua Chen[1@], Michael J. Kleeman[2], Hongliang Zhang[2], Steven P. DeNero[2], and David K. Joe[2]

[1] Department of Land, Air, and Water Resources, University of California, Davis, CA

[2] Department of Civil & Environmental Engineering, University of California, Davis, CA

Submitted to

Atmospheric Chemistry and Physics

October 18, 2015

[@]Corresponding author address: Dr. Shu-Hua Chen, Department of Land, Air, and Water Resources, University of California, Davis, California 95616-8627.
E-mail: shachen@ucdavis.edu

*now at: Singapore-MIT Alliance for Research and Technology (SMART), Centre for Environmental Sensing and Modeling (CENSAM), Singapore

Abstract

The source-oriented Weather Research and Forecasting chemistry model (SOWC) was modified to include warm cloud processes and applied to investigate how aerosol mixing states influence fog formation and optical properties in the atmosphere. SOWC tracks a 6-dimensional chemical variable (X, Z, Y, Size Bins, Source Types, Species) through an explicit simulation of atmospheric chemistry and physics. A source-oriented cloud condensation nuclei module was implemented into the SOWC model to simulate warm clouds using the modified two-moment Purdue Lin microphysics scheme. The Goddard shortwave and longwave radiation schemes were modified to interact with source-oriented aerosols and cloud droplets so that aerosol direct and indirect effects could be studied.

The enhanced SOWC model was applied to study a fog event that occurred on 17 January 2011, in the Central Valley of California. Tule fog occurred because an atmospheric river effectively advected high moisture into the Central Valley and nighttime drainage flow brought cold air from mountains into the valley. The SOWC model produced reasonable liquid water path, spatial distribution and duration of fog events. The inclusion of aerosol-radiation interaction only slightly modified simulation results since cloud optical thickness dominated the radiation budget in fog events. The source-oriented mixture representation of particles reduced cloud droplet number relative to the internal mixture approach that artificially coats hydrophobic particles with hygroscopic components. The fraction of aerosols activating into CCN at a supersaturation of 0.5% in the Central Valley decreased from 94% in the internal mixture model to 80% in the source-oriented model. This increased surface energy flux by 3-5 W m^{-2} and surface temperature by as much as 0.25 K in the daytime.

1. Introduction

Atmospheric aerosols are complex mixtures of particles emitted from many different anthropogenic and natural sources suspended in the atmosphere. In contrast to greenhouse gases, aerosols have large spatial and temporal variability in the troposphere because of their short lifetimes (about one week) before coagulation, dry deposition, or wet scavenging processes remove them from the atmosphere (Ramanathan et al., 2001). Aerosol particles can influence human health (McMichael et al., 2006), ecological health (over land and ocean) (Griffin et al., 2001), visible range through the atmosphere (Dick et al., 2000), cloud / precipitation formation (Chen et al., 2008), and the net radiation budget of the earth (IPCC, 2007). Some chemical components of aerosol particles are important to direct radiative forcing of the climate due to their optical properties (Tegen et al., 1996). Particulate sulfate scatters incoming solar radiation, leading to an estimated direct forcing of -0.95 W m^{-2} (Adams et al., 2001). Particulate black carbon strongly absorbs incoming shortwave radiation, which warms the mid-level of the atmosphere but cools the earth's surface (Yang et al., 2009;Koch and Del Genio, 2010). Particulate black carbon also leads to reduce relative humidity and cloud liquid water content (semi-direct effect) in the mid-level atmosphere (Ackerman et al., 2000; Koch and Del Genio, 2010). In addition to these direct effects, Twomey (1974) proposed that aerosols indirectly affect the earth's energy budget due to their ability to serve as cloud condensation nuclei (CCN), which are of great importance in cloud development, especially for warm clouds in the mid-to-high latitudes. Large numbers of CCN produce clouds with a greater number of smaller size cloud droplets (Chen et al., 2008). These smaller cloud droplets raise cloud albedo (the first indirect effect) and also suppress the formation of precipitation and prolong cloud lifetime (the second indirect effect) (Albrecht, 1989). The direct, semi-direct, and indirect effects of aerosol particles modify the energy budgets in the atmosphere and on the surface, with corresponding changes in

atmospheric stability. The 2007 IPCC report (IPCC, 2007) concluded that the net forcing of all aerosols could be either positive or negative in the range from -0.7 W m^{-2} to +0.1 W m^{-2}. The majority of this uncertainty is associated with the semi-direct and indirect effects due to the complexity of aerosol-cloud interactions.

The magnitude of the aerosol semi-direct and indirect effects depends on the number concentration, size, and composition of the atmospheric aerosol particles that act as CCN or ice nuclei (IN) (Lohmann and Feichter, 2005; Chen et al., 2008). Particles with hygroscopic components such as water-soluble ions (Na^+, Cl^-, SO_4^{2-}, NO_3^- etc.) readily act as CCN (Chen and Lamb, 1994). Particles that contain hydrophobic components such as freshly emitted organic carbon or elemental carbon must become coated with hygroscopic material before they will easily serve as CCN (Dusek et al., 2006). This aging process is often parameterized in models (Lesins et al., 2002) but little information is available to describe how the aging timescale should respond to changes in temperature, humidity, oxidant concentrations and/or emissions rates. Mineral dust particles (Motoi, 1951; Georgii and Kleinjung, 1967) commonly have a favorable arrangement of surface structure that allows them to serve as IN. Secondary coatings that condense on mineral dust particles may reduce their ability to serve as IN (Sullivan et al., 2010) but increase their ability to serve as CCN (Li and Shao, 2009). All of these effects point to the importance of the particle mixing state when predicting CCN / IN concentrations.

The standard Weather Research and Forecasting (WRF) model, including the chemistry component (WRF/Chem), permits the simulation of the combined direct, indirect and semi-direct effects of aerosols (Chapman et al., 2009;Fast et al., 2006;Grell et al., 2005). WRF/Chem Version 3.1.1 has sophisticated packages to represent chemistry processes (i.e. gas-phase reaction, gas-to-particle conversion, coagulation, etc.) and aerosol size and

composition (Zaveri et al., 2008;Ackermann et al., 1998;Binkowski and Shankar, 1995;Schell et al., 2001). The Modal Aerosol Dynamics Model for Europe with Secondary Organic Aerosol Model (MADE-SORGAM) and the Model for Simulating Aerosol Interactions and Chemistry (MOSAIC) are commonly used aerosol schemes in the WRF/Chem model. Both schemes have inorganic, organic, and secondary organic aerosols and contain aerosol formation processes including nucleation, condensation, and coagulation. The main difference between MADE-SORGAM and MOSAIC is the representation of aerosol size distributions. MADE-SORGAM uses 3 log-normal modes (Aitken, accumulation and coarse) while MOSAIC uses 4 (or 8) aerosol size sections (bins) from 39 nm to 10 μm, respectively. The details of MADE-SORGAM are described in Binkowski and Shankar (1995), Ackermann et al. (1998), Schell et al. (2001), and Grell et al. (2005) and the details of MOSAIC are given in Zaveri et al. (2008).

As mentioned above, the size, composition, and mixing state of aerosols strongly affect their ability to activate into cloud droplets (Lance et al., 2013;Zaveri et al., 2010). However, most WRF/Chem chemistry packages make a global internal mixing assumption in which all particles within a log-normal mode (MADE-SORGAM) / size bin (MOSAIC scheme) in the same grid cell are instantaneously combined such that they have the same chemical composition. In reality, airborne particles are emitted with unique chemical composition and only become internally mixed over a period of hours to days depending on atmospheric conditions. The instantaneous internal mixing assumption alters the optical and chemical properties of particles in WRF/Chem simulations (Zhang et al., 2014) and therefore has the potential to influence aerosol-cloud interaction (i.e. CCN activation).

The primary goal of this research is to quantify the effect of assumptions about particle mixing state on predicted cloud droplet formation within the WRF/Chem model. Warm

cloud processes in the Purdue Lin scheme (Chen and Sun, 2002) were modified in the Source-Oriented WRF/Chem (SOWC) model to investigate the impact of aerosol mixing state on the characteristics of a fog event in the Central Valley of California. The SOWC model explicitly predicts particle mixing state in the presence of emissions, transport, coagulation, chemical transformation, and deposition. The integration of warm-cloud processes with the source-oriented treatment of particles in the current study provides a more realistic approach to understand how mixing state influences direct, indirect, and semi-indirect effects of anthropogenic aerosols.

This paper is organized as follows: the model description and development of warm cloud processes are introduced in section 2; observational data and numerical experiment design are presented in section 3; results are discussed in section 4; and the summary and discussion are provided in section 5.

2. Model Description and Development

2.1 SOWC

WRF is a compressible, non-hydrostatic regional meteorology model, which uses the Arakawa C grid and terrain-following hydrostatic pressure coordinates. The governing equations of the model are written in flux form and can be solved using a range of solution schemes. In the present study, the Runge-Kutta third-order time scheme was employed and fifth- and third-order advection schemes were chosen for the horizontal and vertical directions, respectively (Skamarock et al., 2008). WRF/Chem simulates trace gas and particle chemical concentrations concurrently with the meteorological fields using the same grid structure, the same advection scheme, and the same physics schemes for sub-grid scale transport (Grell et al., 2005). The SOWC model was developed based on WRF/Chem V3.1.1 with significant modifications throughout the code to enable the use of 6D variables. The

standard WRF/Chem model tracks 3-dimensionial chemistries in a 4-dimensional variable (X, Z, Y, Species). The SOWC model tracks a 6-dimensional chemical variable "AQC" (X, Z, Y, Size Bins, Source Types, Species). Particles emitted from different sources have different sizes and chemical compositions, leading to a source-oriented mixture of particles that age in the atmosphere through coagulation and gas-particle conversion (e.g., condensation and evaporation) processes. Airborne particles in the SOWC model influence meteorological conditions through radiative feedbacks and microphysical processes. The model simultaneously tracks particle mass, number concentration, and radius. The number concentration and radius of different particle size bins from each source type are included as the last two elements in the species dimension. Simulations in this study use 38 chemical species (Table 1) from 5 emissions sources (wood smokes, gasoline, diesel, meat cooking, and other aerosol types) and 8 size bins. The initial particle sizes from emissions are 0.005, 0.1105, 0.221, 0.4415, 0.8835, 1.767, 3.535, and 7.0693 microns. Note that the SOWC model uses moving size bins whose sizes change in response to gas-particle conversion during model simulations. The model conserves aerosol mass concentration throughout the simulation of atmospheric processes including emissions, transport, deposition, coagulation, and condensation/evaporation. The gas-phase species emitted from different sources in each grid cell are not tracked separately in the SOWC model at the present time. In the current study, the initial and boundary conditions of aerosol particles are based on observations from the California Regional Particulate Air Quality Study (CRPAQS) (Ying et al., 2008). The distribution of particle emissions for different bins for every source are calculated using emissions inventories provided by the California Air Resources Board (CARB) along with measured chemical speciation profiles (Ying et al., 2008). Further details of the SOWC model structure and source-oriented chemistry processes are described by Zhang et al. (2014) and Joe et al. (2014).

177 **2.2 Cloud microphysics scheme**

178 The original Purdue Lin microphysics scheme was designed as a one-moment water
179 mass conserved microphysics scheme with five hydrometeors: cloud water, rain, cloud ice,
180 snow, and graupel (Lin et al., 1983;Chen and Sun, 2002). Chapman et al. (2009) added a
181 prognostic treatment of cloud droplet number (Ghan et al., 1997) to the Purdue Lin scheme to
182 make a two-moment treatment of cloud water within WRF/Chem. In our study, a source-
183 oriented CCN module was added to the SOWC model to track size-resolved information
184 about activated CCN from various aerosol sources. A new source-oriented 6D cloud
185 variable, "CLDAQC" (X, Z, Y, Size Bins, Source Types, Species) was added to SOWC to
186 describe source-oriented clouds. Droplet radius and number concentration are once again
187 stored as the last two elements in the species dimension of the CLDAQC variable. In the
188 Purdue Lin scheme, all microphysics processes are parameterized with water mass, except
189 autoconversion. Chapman et al. (2009) added the autoconversion parameterization from Liu
190 et al. (2005) into the Purdue Lin microphysics, which depends on cloud droplet number.
191 Chapman et al. (2009) also specified changes to cloud droplet number proportional to the
192 microphysics process rate of cloud water mass. For example, when 10% cloud water
193 becomes rain water after autoconversion, 10% cloud droplets will be moved at the same time.

194 The continuity equation of the mass-coupled mixing ratio of CLDAQC can be written as
195 follows:

196 $$\frac{\partial CLDAQC}{\partial t} = \nabla \cdot \vec{V} CLDAQC + \nabla \cdot K \nabla CLDAQC + P_{AACT} + S_{micro}, \quad (1)$$

197 where $\vec{V}$ is the 3D wind vector and *K* is the eddy diffusion coefficient. The first two terms on
198 the right hand side of Eq. (1) are the flux divergence of CLDAQC (transport) and sub-grid
199 eddy mixing, respectively. Figure 1 shows the schematic diagram of the sinks and sources of

CLDAQC in the cloud microphysics processes (P_{AACT} and S_{micro}). Aerosol activation (P_{AACT}) is the main source of CLDAQC. The calculation of aerosol activation is based on a maximum supersaturation determined from a Gaussian spectrum of updraft velocities and aerosol chemistry composition for each size bin (Abdul-Razzak and Ghan, 2002). This parameterization of aerosol activation was implemented in WRF/Chem model (Chapman et al., 2009) and is used in this study. Aerosol activation was calculated each time step. Once the environment reached the critical supersaturation, AQC activated as CCN. Water vapor condenses at a diffusion limited rate to cloud droplets (water molecules transferred from vapor to cloud in Purdue Lin scheme) and particle mass/number is transferred from the interstitial aerosol variable (AQC) to the cloud-borne aerosol variable (CLDAQC). The Purdue Lin microphysics scheme uses a saturation adjustment approach (i.e., it adjusts water vapor to the saturation mixing ratio), so CCN activation is calculated before saturation adjustment. After saturation adjustment, the condensation rate due to vapor diffusion is proportional to particle size (Rogers and Yau, 1989). Results from CCN activation tests at relevant supersaturation are discussed in Section 4.3.

Sinks and sources of CLDAQC (S_{micro}) are based on interactions between a cloud droplet and the other hydrometeors (e.g., ice, rain, snow, and graupel) that can remove water from or add water to CLDAQC. The sinks of cloud water, as well as CLDAQC, include autoconversion from cloud to rain (P_{RAUT}) and the accretion of cloud water by rain (P_{RACW}), snow (P_{SACW}), and graupel (P_{GACW}). The exchange between cloud water and cloud ice can also occur through homogenous freezing of cloud water to ice (P_{IHOM}) and melting of cloud ice to cloud water (P_{IMLT}). Finally, the condensation (associated with P_{ACCT}) and evaporation of cloud water (P_{CEVP}) are implicitly taken into account in the Purdue Lin microphysics scheme. When cloud droplets fully evaporate (sink of CLDAQC), the residual cores are released back into the corresponding source type and size bin of the aerosol (AQC) variable.

225 **2.3 Radiation schemes**

226 The NASA Goddard shortwave and longwave radiation schemes (Chou and Suarez,
227 1999b, 2001b) are used in conjunction with the source-oriented cloud droplet algorithms in
228 the enhanced SOWC model. Absorption of radiation by water vapor, ozone, oxygen, carbon
229 dioxide, cloud droplets and aerosol particles is considered. Interactions among the absorption
230 and scattering by clouds and aerosols (Mie scattering), molecules (Rayleigh scattering) and
231 the surface are fully accounted for (Skamarock et al., 2008). Three main optical parameters
232 are calculated for each model layer to describe the influence of aerosols on the radiation:
233 aerosol optical thickness (τ), single scattering albedo (ω), and asymmetry factor (g). In the
234 present study, the numerical code described by Ying and Kleeman (2003) was implemented
235 to calculate the optical properties of source-oriented particles. The original numerical code
236 of Mie scattering developed by Bohren and Huffman (1983) was used to calculate the particle
237 extinction efficiency, scattering efficiency and asymmetry factor. The partial molar
238 refractive index approach described in Stelson (1990) was used to estimate the mean
239 refractive index for multi-component aerosols. .

240 For any wavelength of shortwave or longwave radiation (λ), the aerosol optical thickness
241 (τ_a) of a model layer with depth h (m) containing a number concentration $n_a(r)$ (# m^{-3} μm^{-1})
242 of droplets with radius r (μm) is given by

243 $$\tau_a(\lambda) = \pi h \int_0^\infty Q_e(\lambda, r) r^2 n_a(r)\, dr, \quad (2)$$

244 where, Q_e is the dimensionless extinction efficiency. The equivalent definition of aerosol
245 optical thickness for discrete size bins j with a mean radius r_j (μm) can be written as

246 $$\tau_a(\lambda) = \pi h \sum_i^n \sum_j^m Q_{ei,j}(\lambda, r) {r_{i,j}}^2 N_{i,j}, \quad (3)$$

where subscript *i* refers to emission source, subscript *j* refers to size, *n* is the number of particle source types and *m* is the number of particle sizes. *N* (# m^{-3}) is the number of particles. The mean asymmetry factor (g_a) and single scattering albedo (ω_a) are calculated using the method described in (Yang, 2000):

$$g_a(\lambda) = \frac{\sum_i^n \sum_j^m Q_{si,j}(\lambda,r) g_{i,j}(\lambda,r) N_{i,j} \pi r_{i,j}^2}{\sum_i^n \sum_j^m Q_{si,j}(\lambda,r) N_{i,j} \pi r_{i,j}^2}, \quad (4)$$

$$\omega_a(\lambda) = \frac{\sum_i^n \sum_j^m Q_{si,j}(\lambda,r) N_{i,j} \pi r_{i,j}^2}{\sum_i^n \sum_j^m Q_{ei,j}(\lambda,r) N_{i,j} \pi r_{i,j}^2}, \quad (5)$$

where Q_s is the dimensionless scattering efficiency. All of the optical parameters are functions of the wavelength (λ) of incident radiation.

In the original Goddard radiation schemes, cloud droplets are assigned to a mono-disperse size distribution (mean effective radius) which depends on the water mass and number concentration. The source-oriented cloud (CLDAQC) contains size distribution and chemistry information which is more realistic than the mono-disperse assumption. Equations 3-5 are applied to all size bins of not only the AQC but also the CLDAQC variables to calculate optical properties and radiative forcing.

3. Numerical experiment designs

3.1 Fog event

A numerical simulation of fog was carried out with the SOWC model as a convenient method to test the effects of particle mixing state on warm clouds processes. The influence of particle size and composition on fog formation and droplet growth has been studied in previous field experiments (Frank et al., 1998;Moore et al., 2004;Ming and Russell, 2004;Cubison et al., 2008;Niu et al., 2012) and modeling studies (Bott and Carmichael, 1993;Kleeman et al., 1997). The results indicate that particle chemical composition and

mixing state strongly influence fog droplet activation, mirroring the processes of interest for cloud droplets.

Tule fogs (radiation fog) frequently form in the Central Valley of California during the winter season (Hayes et al., 1992). Winter in the Central Valley is associated with the maximum concentration of airborne particulate matter (PM) (Chow et al., 1993) which is composed of aerosol particles that can act as CCN. We chose this challenging weather system for the first study of this kind since Tule fog is important in safety, hydrology and agriculture in California. Fog is also an excellent scientific case study that can isolate cloud activation and diffusive growth, the first step of aerosol-cloud-radiation interactions, from other microphysical processes which usually do not occur in fog. In the present study, a thick fog event that occurred on 16 and 17 January 2011 (Fig. 2) was chosen to investigate the impact of source-oriented aerosol-cloud-radiation interactions on fog formation. Fog started forming over the northern Central Valley on 13 January with observed surface relative humidity reaching 95-100% and extended to the southern Central Valley on 14 January. The fog became thicker on 16 January and reached the maximum on 17 January (Fig. 2). This is evident by retrieved cloud optical thickness from MODIS (discussed later). The fog started dissipating from the northern Central Valley on 18 January and fully dissipated on 19 January (Fig. 2c).

In addition to calm wind and radiative cooling, high moisture is an important ingredient to a Tule fog event in the Central Valley, California. Figure 3 shows the time series of column integrated water vapor, sea level pressure, and 850-hPa wind vectors from ECMWF Interim reanalysis data. On 11 January, the column water vapor (CWV) was very low, less than 10 mm, over the Central Valley (Fig. 3a). Moisture was advected into the Central Valley (Fig. 3b) by a winter cyclone moving close to the northwestern coast of the United Sates on 12 January. A weak southwest-northeast-oriented atmospheric river with a width of

1000 km and a maximum CWV of ~26-28 mm approached the western coast and brought moisture into the Central Valley. At 0000 UTC 13 January (Fig 3c), moisture content began increasing in the northern Central Valley. At night, drainage flow from the surrounding mountains brought cold air into the Central Valley, mixed with the low-level moist air, and initiated fog formation over the northern Central Valley. On 14 January (Fig. 3d), the CWV over the southern Central Valley reached 22-24 mm and fog formed over the southern Central Valley.

On 15 and 16 January, a more intense, west-southwest to east-northeast oriented atmospheric river advected moisture into northern California (Figs. 3e and f). The moisture in the Central Valley reached a maximum on 17 January (Fig. 3g), at the time when the fog reached its maximum thickness during the study period (Fig. 2; also see the cloud optical thickness discussion later). On 18 January (Fig. 3h), while high moisture and fog still presented over the southern Central Valley, the moisture decreased and the fog disappeared over the northern Central Valley. Fog fully dissipated in the Central Valley on 19 January.

According to the satellite images and surface temperature variation, the coverage and thickness of fog followed a diurnal pattern with thinning in the daytime and thickening at night. As mentioned earlier, the aerosol mixture state can impact fog formation and properties of cloud droplets.

3.2 Observational data

Multiple types of measurement data were used to evaluate the SOWC model performance. Moderate Resolution Imaging Spectroradiometer (MODIS) level 2 cloud products from the Terra and Aqua satellites provide 5-km resolution cloud optical thickness (COT) and liquid water path (LWP). The LWP retrieval from MODIS has been used to study low cloud and fog (Bendix et al., 2005). High-resolution MODIS data can describe fog spatial distribution and intensity but are only available once every 24 hours (daytime only)

from each satellite. The SOWC model predictions for temperature and moisture at the surface are also evaluated against *in situ* time-series meteorological data from 24 surface weather stations along with net ground shortwave fluxes at 42 sites from California Irrigation Management Information System (CIMIS). Measured concentrations of airborne particles were obtained from the California Ambient Air Quality Data (CAAQD) provided by the Planning & Technical Support Division (PTSD) of the California Air Resources Board (CARB). The station details of CAAQD are provided in Table 2. The locations of all measurement sites are provided in Fig. 4.

3.3 Numerical experiment design

The primary objective of this study is to examine how the source-oriented (S_) and internal (I_) mixture representations of aerosol particles differ in their feedbacks to meteorology in a fog event. Internally mixed simulations (I_) artificially blend emissions from all sources into a single particle size distribution thereby concealing all advanced treatments of particle mixing and aging. Four experiments were carried out (Table 3) for the selected fog event. In the basecase experiment of S_ARon_CRmod, the polluted aerosol particles tracked by AQC act as the source of CCN (S_) and the aerosol-radiation interaction (aerosol direct effect) is enabled in the radiation schemes (ARon). The geometric-optics approach mentioned in Section 2.3 is used to calculate the cloud optical properties of each model layer (CRmod). S_ARon_CRorig is similar to S_ARon_CRmod, except for the use of the original cloud optical property calculation (CRorig) in the NASA Goddard shortwave and longwave radiation schemes. As discussed previously, the original schemes are based on an estimate of the cloud droplet effective radius using the cloud mass and number concentration (CRorig). The radius of cloud droplets in the original Goddard shortwave radiation scheme is constrained to the range from 4 μm to 20 μm. In the modified cloud-radiation scheme (CRmod), the size range of cloud droplets in Eq. (3) can vary between the dry aerosol particle

radius to 30 μm. S_ARoff_CRmod has no aerosol direct effect in the radiation schemes (ARoff). The comparison of S_ARoff_CRmod and S_ARon_CRmod is used to estimate the aerosol direct effect in this study.

Each numerical experiment employed two domains with two-way nesting. Domain 1 (86 x 97 grid cells) had a resolution of 12 km while domain 2 (127 x 202 grid cells) had a resolution of 4 km. Domain 2 was positioned to cover the entire Central Valley of California and results from this domain are used for the subsequent analysis. All simulations used 31 vertically staggered layers based on a terrain-following pressure coordinate system. The vertical layers are stretched with a higher resolution near the surface (an average depth of ~30 m in the first model half layer). Variables other than vertical velocity and geopotential were stored in the half model levels. The time step was 60 seconds for the first domain and 20 seconds for the second domain. The physics schemes employed for the simulations included the modified Purdue Lin microphysics scheme (Chen and Sun, 2002), the NASA Goddard longwave/shortwave radiation schemes (Chou and Suarez, 1999a, 2001a), the Kain-Fritsch cumulus scheme (Kain and Fritsch, 1990;Kain, 1993) (domain 1 only), the YSU PBL scheme (Hong et al., 2006;Hong, 2010) and the Noah LSM surface scheme (Tewari et al., 2007). No cumulus scheme is used in the inner-most domain (4 km resolution). The number of cloud droplets was not considered in the convective scheme in the SOWC model. The target episode had calm winds with local fog formation in the Central Valley (not propagating in through lateral boundaries). Moreover, the event occurred in the winter season when the Convective Available Potential Energy (CAPE) was small. Therefore, the KF cumulus convective parameterization is inactive for this cases study. The meteorological initial and boundary conditions were taken from North American Regional Reanalysis (NARR), which has a spatial resolution of 32 km and a temporal resolution of 3 hours.

368 The SOWC model tracked two 6D variables for aerosol/cloud properties which
369 introduce considerable computational burden for model simulations when compared to
370 standard WRF/Chem model simulation (with prescribed aerosol concentration). The
371 computational cost of the SOWC model, which is proportional to the extra information that is
372 tracked, is approximately 25 times greater than the standard WRF/Chem 3.1.1 simulation
373 with prescribed aerosols (chem_opt = 0) or approximately 5 times greater than the standard
374 WF/Chem 3.1.1 simulation with any chemistry option (/=0) in the current study. SOWC
375 model simulations started at 0000 UTC 9 January (7 days prior to the start of the thick fog
376 event) with four-dimensional data assimilation (FDDA), which nudges model fields in
377 domain 1 to analysis including the u and v components of horizontal winds, water vapor
378 mixing ratio, and temperature above the PBL height in all simulations. This approach
379 provides a realistic heterogeneous aerosol distribution and low-level temperature and
380 moisture fields at the start of the thick fog simulation. Observations from surface stations
381 and NARR data were used for nudging during this aerosol spin-up period. Between 0000
382 UTC 16 January to 0000 UTC 19 January, the SOWC model integrated without FDDA (3
383 day free run) during which time the effects of the different model configurations were
384 observed and is our major interested time period.

385 **4. Model Results**

386 **4.1 Evaluation of basecase (S_ARon_CRmod) model performance**

387 The SOWC model calculates CCN number concentrations based on the activation of
388 aerosols (AQC). The AQC number concentration can influence the intensity of initial fog
389 formation and spatial distribution of final fog fields, and thus AQC number concentration is
390 examined first. Figure 5 shows 72-hour averaged (from 16 to 18 January 2011) AQC number
391 concentrations in California's Central Valley that were also averaged over the first five model
392 layers for S_ARon_CRmod. Fog usually forms within the planet boundary layer (PBL),

393 which reaches to a height of approximately five model layers in winter conditions in the
394 Central Valley (450-550 m). Temporally averaged AQC concentrations are approximately
395 2×10^9 # m^{-3}, with the highest concentrations predicted in the vicinity of polluted cities (e.g.,
396 the San Francisco Bay Area, Stockton, Modesto, Sacramento, Fresno, and Bakersfield), in the
397 middle of the Central Valley, and at foothills of Sierra Nevada Mountain over the east-
398 southeastern Central Valley.

399 Figure 6 shows the comparison of simulated nitrate (NO_3^-), sulfate (SO_4^{2-}), ammonium
400 (NH_4^+) and soluble sodium (Na^+) concentrations to measured values at 6 monitoring stations
401 (see Table 2 and Fig. 4) on 18 January 2011. Simulated sulfate and soluble sodium are in
402 reasonable (>80%) agreement with measurements but nitrate and ammonium concentrations
403 were under predicted by approximately 70%. The cause for this discrepancy is unknown, but
404 one possibility is the presence of organic nitrate compounds in the atmosphere that are not
405 simulated by the model chemistry. Note that both observed and predicted nitrate
406 concentrations in the current episode are lower than the maximum concentrations observed in
407 historical extreme episodes within the San Joaquin Valley (SJV) because the current
408 stagnation event only lasted a few days while extreme events last multiple weeks. If more
409 discussion of aerosol perditions form the SOWC model is desired, we refer the reader to
410 Zhang et al. (2014) who present a comparison of predicted aerosol concentrations and
411 measured concentrations using field campaign data measured during the California Regional
412 PM_{10} / $PM_{2.5}$ Air Quality Study (CRPAQS) in December 2000 – January 2001.

413 The S_ARon_CRmod experiment reasonably reproduces the observed spatial
414 distribution and magnitude of liquid water path (LWP) compared to the data retrieved from
415 MODIS (Fig. 7). In particular, the model predicts LWP well over the northern portion of the
416 Central Valley during the fog event (16 to 18 January). However, the model under-predicts
417 LWP in the middle portion of the Central Valley, which caused the fog to dissipate earlier

418 (late 17 January). Once the surface temperature increases in one area due to thin fog, the
419 dissipation spreads out quickly until the fog completely evaporates. For the southern portion
420 of the Central Valley, the fog event starts earlier (14 to 15 January) and the model reasonably
421 predicts the onset of the event. But the simulated fog is too dense (figure not shown). In
422 addition, the peak of the simulated fog occurs one day earlier (16 January forecast versus 17
423 January observed). This timing difference could be caused by the change in the microphysics
424 processes at 0000 UTC 16 January. During the FDDA time period (before 16 January), the
425 one-moment bulk microphysics scheme is used. After the FDDA time period, aerosols start
426 being involved in cloud formation. High Nitrate concentrates in the SJV and enhances
427 aerosol activation due to its high hygroscopicity. This could partially explain why the peak
428 of the LWP occurs on 16 January. The details of aerosol chemical properties are discussed
429 by Zhang et al. (2014).

430 While simulated LWP is comparable to MODIS retrievals with one day shift (Fig. 7),
431 high CCN concentration and smaller cloud droplets, thus high COTs (Fig. 8), are predicted in
432 the SOWC simulations especially in highly polluted areas. High predicted COT results in
433 cold surface temperature, especially in the southern portion of the Central Valley. Overall,
434 the spatial distribution and magnitude of simulated COT also match the satellite data
435 reasonably (Fig. 8), except for the overestimation of COT over the southeastern Central
436 Valley (Fig. 8b and d).

437 Mean biases of 2-m temperature (T2), 2-m water vapor mixing ratio (Q2), and surface
438 net downward shortwave radiative flux (NSF) over the entire Central Valley from 16 to 18
439 January 2011 for S_ARon_CRmod are calculated (Fig. 9). Generally, T2 and Q2 of
440 S_ARon_CRmod are under-predicted by 2 °C and 0.7 g kg^{-1}, respectively. The predicted
441 time variation of T2 and Q2 biases is small in the first one and half days but increases after
442 1600 UTC 17 January because the predicted fog dissipated in the daytime, different from

observations. Since the predicted fog dissipated, simulated NSF increased and was over-predicted by 13.9 W m^{-2}. Low simulated T2 and Q2, particularly during first one and half days, in S_ARon_CRmod are partially due to over-predictions of the fog formation (i.e., too much condensation leading to depleted water vapor), especially over the southern portion of the Central Valley. Overall, S_ARon_CRmod reasonably forecasted LWP and COT spatial pattern and intensity. S_ARon_CRmod also captured the diurnal pattern of T2 and Q2 during the fog event, but under-predicted the absolute magnitude of T2 and Q2 by 1.76 (2.22) °C and 0.56 (0.88) g kg^{-1} in the daytime (nighttime), respectively.

4.2 Source-oriented aerosol direct and indirect effects

S_ARoff_CRmod is designed to test aerosol-radiation feedback and so the comparison between S_ARoff_CRmod and S_ARon_CRmod can help quantify the aerosol direct effect in the current study. Table 4 shows that the hourly bias mean and standard deviation from 24 surface stations in the daytime and nighttime of S_ARoff_CRmod are similar to, but larger than, results from S_ARon_CRmod for T2 and Q2 at the ground. However, compared to S_ARon_CRmod, the smaller cold bias from S_ARoff_CRmod is consistent with its larger net downward shortwave radiative flux (NSF) shown in Tables 4 and 5. Table 5 shows that the average NSF within the entire Central Valley from S_ARoff_CRmod is higher than S_ARon_CRmod by 3.7 W m^{-2}, which means that the shortwave energy flux that reached the ground was reduced by ~3.7 W m^{-2} due to aerosol radiative forcing in this case study. The maximum increases of T2 and NSF by the aerosol direct effect occurred on 17 January 2011 (Fig. 9). Table 5 also shows the mean value of cloud water mixing ratio, cloud droplet number, surface skin temperature, latent heat flux and sensible heat flux over the Central Valley during 16 to 18 January 2011. Cloud water mixing ratio and cloud droplet number were averaged within the first five model layers. The aerosol direct effect leads to increases

in the cloud water mass and cloud droplet number by 3.3% and 4.5%, respectively, due to reductions in skin temperature (0.1 K) and net shortwave flux (3.7 W m^{-2}).

The modified radiation schemes for cloud optical properties in the S_ARon_CRmod experiment do not have significant feedback on spatially and temporally averaged cloud water mass and cloud droplet number (i.e., compared to S_ARon_CRorig) as shown in Table 5. Theoretically, the modified cloud-radiation interaction (i.e., geometric-optics method) used in the COT calculations (S_ARon_CRmod) can predict higher COT which leads to slightly lower net shortwave flux and surface skin temperature, especially in the polluted area. The higher COT predictions are likely caused by differences in the size range of cloud droplets and refractive indexes of cloud water with/without chemical composition in the calculation of cloud radiative properties. As mentioned above, the radius of cloud droplets in the original Goddard shortwave radiation scheme is constrained to the range from 4 μm to 20 μm, while in our modified radiation scheme, the cloud droplets are allowed to range in size between the dry aerosol particle radius to 30 μm. The parameterization of cloud optical thickness in the original Goddard radiation scheme assumes that cloud droplets are pure water. The modified scheme recognizes the chemical species in the cloud water and considers these species when calculating the cloud droplet index of refraction. However, in this case study the results of these two experiments (i.e., S_ARon_CRmod and S_ARon_CRorig) were very similar. Because the meteorological conditions of the fog event are calm and stable, the cloud microphysics processes are fairly slow and simple (no rain produced in this case). Although S_ARon_CRorig had slightly higher cloud droplet number concentrations, the modified calculation of the cloud optical properties in S_ARon_CRmod gave a similar cloud amount and net shortwave radiation flux reaching the surface, which produced nearly identical feedbacks to meteorology in both experiments (Table 5).

4.3 Internal mixture versus source-oriented aerosols

The mixing state of chemical components among the atmospheric aerosol particles can potentially play an important role in fog formation. The activation of aerosol particles into cloud droplets depends on the critical super-saturation which in turn depends on particle composition. According to the Köhler equation, increased concentrations of solutes will decrease the critical super-saturation required to activate a particle into a CCN. As mentioned earlier, hydrophobic particles (i.e. black carbon) will more easily serve as CCN once they are coated with hygroscopic material (i.e. sulfate). Increased concentrations of solutes can potentially modify the frequency and severity of fog events in polluted air. In this section, we compare results from S_ARon_CRmod (source-oriented experiment) and I_ARon_CRmod (internally mixed experiment) to investigate the activation change and further meteorological responses between internally mixed and source-oriented aerosols. The internally mixed experiment is conducted by lumping all sources together (i.e., AQC source dimension collapsed to one producing a 5D AQC variable).

It is likely that the ratio of CCN concentration (N_{CCN}) to total aerosol concentration (N_{CN}) will be different for each of the five source types tracked in S_ARon_CRmod since the CCN activation depends on the chemical composition and size of the particles. The highest ratio of N_{CCN}/N_{CN} for S_ARon_CRmod and I_ARon_CRmod is located in the southern Central Valley (Fig. 10) due to higher moisture from the atmospheric river resulting in greater aerosols activation to CCNs and smaller residual aerosol number concentration (see Fig. 5). Over the Central Valley during 16 to 18 January 2011, the ratio of N_{CCN}/N_{CN} for each source type is 12.63%, 15.60%, 14.89%, 16.80% and 20.21% for wood smoke, gasoline, diesel, meat cooking, and others, respectively (averaged within the first five model layers). Wood smoke is typically a major source of aerosol (~38%) in California's Central Valley during winter stagnation events (see Table 6) and the organic carbon in wood smoke is water-

516 soluble (Dusek et al., 2011) which allows these particles to activate more easily than
517 insoluble particles. However, the majority of the wood smoke particles are located in the
518 smallest size bin, so the ratio of N_{CCN}/N_{CN} for wood smoke is comparable with that of
519 hydrophobic diesel. The source type of "others", which has the highest ratio of N_{CCN}/N_{CN}, is
520 dominated by larger dust particles coated with secondary components such as nitrate and are
521 easier to activate, in contrast to the smaller combustion particles emitted from other tracked
522 sources.

523 The comparison of the average ratio of N_{CCN}/N_{CN} from the first five model layers
524 between S_ARon_CRmod and I_ARon_CRmod is shown on Fig. 10. The spatial patterns
525 produced by both experiments are similar but I_ARon_CRmod has a higher N_{CCN}/N_{CN} ratio,
526 in particular over the northern two thirds of the Central Valley. The largest differences
527 between N_{CCN}/N_{CN} predicted by S_ARon_CRmod and I_ARon_CRmod occur in regions
528 with large emissions of wood smoke (figure not shown). The ratio of N_{CCN}/N_{CN} for both
529 experiments can reach >30% but the highest N_{CCN}/N_{CN} ratio occurs in relatively less polluted
530 regions. The spatially averaged ratio of N_{CCN}/N_{CN} is 16.65% for S_ARon_CRmod and
531 27.49% for I_ARon_CRmod within the Central Valley over the period of 16 to 18 January.
532 The CCN concentrations and N_{CCN}/N_{CN} ratios between internally mixed and source-oriented
533 experiments at different super-saturations were calculated to better understand this result.
534 Figure 11a shows the 72-hour averaged CCN concentration at super-saturations of 0.02%,
535 0.05%, 0.1%, 0.2% and 0.5% and total AQC concentration averaged within the first five
536 model layers. Figure 11b presents corresponding N_{CCN}/N_{CN} ratios at 5 different super-
537 saturations. When the super-saturation is less than or equal to 0.2%, the N_{CCN}/N_{CN} ratio
538 predicted from S_ARon_CRmod is comparable or even slightly higher than that predicted
539 from I_ARon_CRmod. In the S_ARon_CRmod tests, 56% of the particles tracked in the
540 AQC variable (mainly in size bins 2-8) are activated as CCN. When the super-saturation is

close to 0.5%, the N_{CCN}/N_{CN} ratio from I_ARon_CRmod can be 15% higher than that of S_ARon_CRmod. Most particles tracked in AQC size bin 1 can activate in the internally mixed experiment; however, in the source-oriented experiment only particles in AQC size bin 1 associated with wood smoke and "others" sources activate due to the relatively hydrophobic nature of particles associated with other sources (Table 6). Cubison et al. (2008) analyzed observational CCN and CN data in 2005 from a field campaign in California and found that the average ratio of N_{CCN}/N_{CN} was 18% for a super-saturation value of 0.5%, but their predicted N_{CCN}/N_{CN} ratio based on the internal mixture assumptions could reach to more than 50%. In the source-oriented SOWC model, super-saturation values are typically ~0.2-0.3% with maximum value of 0.5% in some areas. The estimated ratio of N_{CCN}/N_{CN} in the source-oriented model is comparable with observations in Cubison et al. (2008), especially in polluted areas. The temporal variations of mean bias of 2-m temperature (T2), 2-m water vapor mixing ratio (Q2), and surface net downward shortwave radiative flux (NSF) between internal versus external aerosol mixture states (I_ARon_CRmod versus S_ARon_CRmod) are similar untill 2000 UTC 17 January. After late 17 January, the bias differences between two experiments are more apparent in the daytime than in the nighttime (Table 4). Compared to I_ARon_CRmod, S_ARon_CRmod reduced bias in T2 by 0.25 K in the daytime but had higher bias in NSF. S_ARon_CRmod did predict improved values of Q2. Based on Fig. 9, we know that the source-oriented and internal aerosol mixing states mainly cause differences in surface temperature in the daytime. Figures 12a and b illustrate the relative change ((internally mixed – source-oriented)/source-oriented * 100%) of averaged (16 - 18 January 2011) cloud water mixing ratio and cloud droplet number, respectively, during the daytime. I_ARon_CRmod predicts cloud water mixing ratios that are 40% higher than values predicted by S_ARon_CRmod over the northern Central Valley (Fig. 12a). The largest relative change in predicted cloud water concentration also occurs in

566 the northern Central Valley near the mountains where fogs are initiated by drainage flow.
567 I_ARon_CRmod predicts higher cloud droplet number (Fig. 12b), with the largest relative
568 increases (~50 - 60%) once again observed in areas near mountains and highly polluted
569 regions with more modest changes of 20~30% over remote regions. Internally mixed
570 aerosols reduce the critical saturation ratio for particles by artificially mixing hygroscopic
571 and hydrophobic components that in turn allows particles to activate more easily.

572 The internally mixed experiment (I_ARon_CRmod) predicts lower daytime averaged
573 surface skin temperature and net downward shortwave flux at ground (Fig. 12c and d)
574 corresponding to the areas with higher cloud water mixing ratio and cloud droplet
575 concentrations (Fig. 12a and b). This result is expected since higher cloud water mixing ratio
576 and cloud droplet concentration will reduce the solar radiation flux on the surface. The
577 reduction of surface skin temperature in the internal mixed experiment is proportional to the
578 change of the net shortwave radiation. Figure 13 shows that the area average of latent heat
579 flux (LH) and sensible heat flux (SH) over the Central Valley in S_ARon_CRmod and the
580 average difference of internally mixed and source-oriented experiments. Higher cloud
581 amount and lower surface temperature are predicted in the internally mixed experiment
582 leading to reduced LH and SH fluxes at ground level compared to the source-oriented
583 experiment. The difference between internally mixed and source-oriented predictions for LH
584 and SH reached 3 W m^{-2} and 5 W m^{-2}, respectively, at noon local time (2200 UTC 17
585 January).

586 Table 7 shows hourly mean bias and root-mean-square-difference between internally
587 mixed (I_ARon_CRmod) and source-oriented (S_ARon_CRmod) experiments for six
588 variables within the Central Valley during 16 to 18 January 2011. The mean bias between
589 these two experiments is 1.19×10^{-2} (g m^{-3}) for cloud water mixing ratio and 6.24×10^{7} (# m^{-3})
590 for cloud droplet number. The direction of these trends is expected since internally mixed

591 aerosols are easier to activate as CCN. The mean bias between internally mixed and source-
592 oriented experiments is -0.15 (K) for surface skin temperature and -6.02 (W m^{-2}) for net
593 shortwave flux. The mean bias of LH and SH is -0.61 and -0.36 (W m^{-2}), respectively. The
594 root-mean-square-difference between these two experiments is large for each variable,
595 meaning that the difference varies strongly with location (see Fig. 12).

596 **5. Summary and discussion**

597 A warm cloud-aerosol interaction module was implemented into the source-oriented
598 Weather Research and Forecasting model with Chemistry (SOWC) to study the aerosol-
599 cloud-radiation interactions during fog simulations. The source-oriented mixture of aerosols
600 is used to explicitly simulate particle aging processes in the atmosphere rather than
601 instantaneously combining particles into an internal mixture. The SOWC model was used to
602 simulate a fog event in California's Central Valley in January 2011 with seven days of FDDA
603 nudging and three days of free run. Fog formation occurred when high moisture content
604 from an Atmospheric River was advected into the Central Valley and cold drainage flows
605 occurred into the valley at night. The initial tests used 5 emissions sources (wood smoke,
606 gasoline, diesel, meat cooking, and others) with particles from each source consisting of 38
607 chemical species and 8 size bins, spanning a diameter range from 0.01 to 10 microns. The
608 highest model spatial resolution was 4 km.

609 Four numerical experiments were conducted to test model performance, meteorological
610 feedbacks from internal and source-oriented aerosols, and the impact of aerosol-cloud-
611 radiation interaction on fog formation. Compared to observations, the SOWC model
612 reasonably predicted fog spatial distribution and duration and environmental meteorological
613 feedbacks. However, the model over-predicted liquid water path and cloud optical thickness,
614 which resulted in cold surface temperature bias. The inclusion of aerosol-radiation
615 interaction reduced net downward shortwave radiative flux by an average of 3.7 W m^{-2} and

daytime surface temperature by 0.1 K. Results that used different treatments for aerosol mixing states were compared, and the important findings are: 1) the fraction of N_{CCN}/N_{CN} at a supersaturation of 0.5% in the Central Valley decreased from 94% in the internal mixture model to 80% in the source-oriented mixture model; 2) due to a smaller number of the CCN concentration in the source-oriented mixture model than in the internal mixture model, cloud water mixing ratio and cloud droplet number decreased 5% and 15%, respectively; and 3) compared to observations, the source-oriented mixture model reduced the cold bias for surface temperature by 0.25 K in the daytime relative to the internal mixture model. The source-oriented mixture representation of particles also provided more reasonable predictions for cloud droplet number and cloud water mass versus observations due to different activation properties than the internal mixture representation of particles. The internal mixture model predicted greater activation of CCN than the source-oriented model due to artificial coating of hydrophobic particles with hygroscopic components.

The SOWC model in this study explicitly calculates primary particle aging over a regional scale for fog formation prediction with two-moment microphysics scheme and aerosol-cloud-radiation interactions. The SOWC model should be a useful tool to study aerosol-cloud-radiation interactions. We are now conducting more numerical studies on different weather systems to explore the full range of responses.

Acknowledgment

The authors would like to acknowledge the WRF and WRF-Chem teams for their efforts on model development. This study was funded by the United States Environmental Protection Agency under Grant No. R833372, NASA Grant No. NNX09AC38G, and NASA High-End Computing (HEC) Program through the NASA Advanced Supercomputing (NAS) Division at Ames Research Center (SMD-13-3895). Although the research described in the article has

been funded by the United States Environmental Protection Agency it has not been subject to the Agency's required peer and policy review and therefore does not necessarily reflect the reviews of the Agency and no official endorsement should be inferred.

References

Abdul-Razzak, H., and Ghan, S. J.: A parameterization of aerosol activation 3. Sectional representation, Journal of Geophysical Research: Atmospheres, 107, AAC 1-1-AAC 1-6, 10.1029/2001jd000483, 2002.

Ackerman, A. S., Toon, O. B., Stevens, D. E., Heymsfield, A. J., Ramanathan, V., and Welton, E. J.: Reduction of Tropical Cloudiness by Soot, Science, 288, 1042-1047, 10.1126/science.288.5468.1042, 2000.

Ackermann, I. J., Hass, H., Memmesheimer, M., Ebel, A., Binkowski, F. S., and Shankar, U.: Modal aerosol dynamics model for Europe: development and first applications, Atmospheric Environment, 32, 2981-2999, http://dx.doi.org/10.1016/S1352-2310(98)00006-5, 1998.

Adams, P. J., Seinfeld, J. H., Koch, D., Mickley, L., and Jacob, D.: General circulation model assessment of direct radiative forcing by the sulfate-nitrate-ammonium-water inorganic aerosol system, Journal of Geophysical Research-Atmospheres, 106, 1097-1111, 10.1029/2000jd900512, 2001.

Albrecht, B. A.: AEROSOLS, CLOUD MICROPHYSICS, AND FRACTIONAL CLOUDINESS, Science, 245, 1227-1230, 10.1126/science.245.4923.1227, 1989.

Bendix, J., Thies, B., Cermak, J., and Nau\ss, T.: Ground fog detection from space based on MODIS daytime data-a feasibility study, Weather and forecasting, 20, 989-1005, 2005.

Binkowski, F. S., and Shankar, U.: The Regional Particulate Matter Model: 1. Model description and preliminary results, Journal of Geophysical Research: Atmospheres, 100, 26191-26209, 10.1029/95jd02093, 1995.

Bohren, C. F., and Huffman, D. R.: Absorption and Scattering of Light by Small Particles, Wiley, New York., 1983.

Bott, A., and Carmichael, G. R.: Multiphase chemistry in a microphysical radiation fog model—A numerical study, Atmospheric Environment. Part A. General Topics, 27, 503-522, http://dx.doi.org/10.1016/0960-1686(93)90208-G, 1993.

Chapman, E. G., Gustafson Jr, W. I., Easter, R. C., Barnard, J. C., Ghan, S. J., Pekour, M. S., and Fast, J. D.: Coupling aerosol-cloud-radiative processes in the WRF-Chem model: Investigating the radiative impact of elevated point sources, Atmos. Chem. Phys., 9, 945-964, 10.5194/acp-9-945-2009, 2009.

Chen, J.-P., and Lamb, D.: Simulation of Cloud Microphysical and Chemical Processes Using a Multicomponent Framework. Part I: Description of the Microphysical Model, Journal of the Atmospheric Sciences, 51, 2613-2630, 1994.

Chen, J.-P., Hazra, A., Shiu, C.-J., Tsai, I.-C., and Lee, H.-H.: Interaction between Aerosols and Clouds: Current Understanding, in: Recent Progress in Atmospheric Sciences: Applicatons to the Asia-Pacific Region, edited by: Liou, K. N., and Chou, M.-D., World Scientific Publishing Co. Pte. Ltd., 231-281, 2008.

Chen, S.-H., and Sun, W. Y.: A one-dimensional time-dependent cloud model, j. Meteor. Soc. Japan, 80, 99-118, 2002.

Chou, M.-D., and Suarez, M. J.: A Solar Radiation Parameterization for Atmospheric Studies NASA Tech. Rep. NASA/TM-1999-10460, 15, 1999a.

686 Chou, M.-D., and Suarez, M. J.: A Thermal Infrared Radiation Parameterization for
687 Atmospheric Studies, NASA Tech. Rep. NASA/TM-2001-104606, 19, 2001a.
688 Chou, M. D., and Suarez, M. J.: A solar radiation parameterization for atmospheric
689 studies., NASA Tech. Rep., 38, 1999b.
690 Chou, M. D., and Suarez, M. J.: A thermal infrared radiation parameterization for
691 atmospheric studies. , NASA Tech. Rep., 55, 2001b.
692 Chow, J. C., Watson, J. G., Lowenthal, D. H., Solomon, P. A., Magliano, K. L., Ziman, S. D.,
693 and Richards, L. W.: PM10 and PM2.5 Compositions in California's San Joaquin Valley,
694 Aerosol Science and Technology, 18, 105-128, 10.1080/02786829308959588, 1993.
695 Cubison, M. J., Ervens, B., Feingold, G., Docherty, K. S., Ulbrich, I. M., Shields, L., Prather,
696 K., Hering, S., and Jimenez, J. L.: The influence of chemical composition and mixing state
697 of Los Angeles urban aerosol on CCN number and cloud properties, Atmos. Chem. Phys.,
698 8, 5649-5667, 10.5194/acp-8-5649-2008, 2008.
699 Dick, W. D., Saxena, P., and McMurry, P. H.: Estimation of water uptake by organic
700 compounds in submicron aerosols measured during the Southeastern Aerosol and
701 Visibility Study, Journal of Geophysical Research: Atmospheres (1984–2012), 105,
702 1471-1479, 2000.
703 Dusek, U., Reischl, G. P., and Hitzenberger, R.: CCN Activation of Pure and Coated Carbon
704 Black Particles, Environmental Science & Technology, 40, 1223-1230,
705 10.1021/es0503478, 2006.
706 Dusek, U., Frank, G. P., Massling, A., Zeromskiene, K., Iinuma, Y., Schmid, O., Helas, G.,
707 Hennig, T., Wiedensohler, A., and Andreae, M. O.: Water uptake by biomass burning
708 aerosol at sub- and supersaturated conditions: closure studies and implications for the
709 role of organics, Atmos. Chem. Phys., 11, 9519-9532, 10.5194/acp-11-9519-2011, 2011.
710 Fast, J. D., Gustafson, W. I., Easter, R. C., Zaveri, R. A., Barnard, J. C., Chapman, E. G., Grell,
711 G. A., and Peckham, S. E.: Evolution of ozone, particulates, and aerosol direct radiative
712 forcing in the vicinity of Houston using a fully coupled meteorology-chemistry-aerosol
713 model, Journal of Geophysical Research: Atmospheres, 111, D21305,
714 10.1029/2005jd006721, 2006.
715 Frank, G., Martinsson, B. G., Cederfelt, S.-I., Berg, O. H., Swietlicki, E., Wendisch, M.,
716 Yuskiewicz, B., Heintzenberg, J., Wiedensohler, A., Orsini, D., Stratmann, F., Laj, P., and
717 Ricci, L.: Droplet Formation and Growth in Polluted Fogs, Contri. Atmos. Phys., 71, 65-
718 85, 1998.
719 Georgii, H. W., and Kleinjung, E.: Relations between the chemical composition of
720 atmospheric aerosol particles and the concentration of natural ice nuclei. , J. Rech.
721 Atmos., 3, 145-156, 1967.
722 Ghan, S. J., Leung, L. R., Easter, R. C., and Abdul-Razzak, H.: Prediction of cloud droplet
723 number in a general circulation model, Journal of Geophysical Research: Atmospheres,
724 102, 21777-21794, 10.1029/97jd01810, 1997.
725 Grell, G. A., Peckham, S. E., Schmitz, R., McKeen, S. A., Frost, G., Skamarock, W. C., and
726 Eder, B.: Fully coupled “online” chemistry within the WRF model, Atmospheric
727 Environment, 39, 6957-6975, http://dx.doi.org/10.1016/j.atmosenv.2005.04.027,
728 2005.
729 Griffin, D. W., Kellogg, C. A., and Shinn, E. A.: Dust in the wind: Long range transport of
730 dust in the atmosphere and its implications for global public and ecosystem health,
731 Global Change and Human Health, 2, 20-33, 2001.
732 Hayes, T. P., Kinney, J. J. R., and Wheeler, N. J. M.: California surface wind climatology,
733 California Air Resources Board, Technical Support Division, Modeling and Meteorology
734 Branch, 1992.

735 Hong, S.-Y., Noh, Y., and Dudhia, J.: A New Vertical Diffusion Package with an Explicit
736 Treatment of Entrainment Processes, Monthly Weather Review, 134, 2318-2341,
737 10.1175/mwr3199.1, 2006.
738 Hong, S.-Y.: A new stable boundary-layer mixing scheme and its impact on the simulated
739 East Asian summer monsoon, Quarterly Journal of the Royal Meteorological Society,
740 136, 1481-1496, 10.1002/qj.665, 2010.
741 IPCC: Climate change 2007-the physical science basis: Working group I contribution to
742 the fourth assessment report of the IPCC, Cambridge University Press, 2007.
743 Joe, D. K., Zhang, H., DeNero, S. P., Lee, H.-H., Chen, S.-H., McDonald, B. C., Harley, R. A.,
744 and Kleeman, M. J.: Implementation of a high-resolution Source-Oriented WRF/Chem
745 model at the Port of Oakland, Atmospheric Environment, 82, 351-363,
746 http://dx.doi.org/10.1016/j.atmosenv.2013.09.055, 2014.
747 Kain, J. S., and Fritsch, J. M.: A one-dimensional entraining/detraining plume model and
748 its application in convective parameterization, Journal of the atmospheric sciences, 47,
749 2784-2802, 1990.
750 Kain, J. S.: Convective parameterization for mesoscale models: The Kain-Fritsch scheme,
751 The representation of cumulus convection in numerical models, Meteor. Monogr, 46,
752 165-170, 1993.
753 Kleeman, M. J., Cass, G. R., and Eldering, A.: Modeling the airborne particle complex as a
754 source-oriented external mixture, Journal of Geophysical Research-Atmospheres, 102,
755 21355-21372, 10.1029/97jd01261, 1997.
756 Koch, D., and Del Genio, A. D.: Black carbon semi-direct effects on cloud cover: review
757 and synthesis, Atmos. Chem. Phys., 10, 7685-7696, 10.5194/acp-10-7685-2010, 2010.
758 Lance, S., Raatikainen, T., Onasch, T. B., Worsnop, D. R., Yu, X. Y., Alexander, M. L.,
759 Stolzenburg, M. R., McMurry, P. H., Smith, J. N., and Nenes, A.: Aerosol mixing state,
760 hygroscopic growth and cloud activation efficiency during MIRAGE 2006, Atmos. Chem.
761 Phys., 13, 5049-5062, 10.5194/acp-13-5049-2013, 2013.
762 Lesins, G., Chylek, P., and Lohmann, U.: A study of internal and external mixing scenarios
763 and its effect on aerosol optical properties and direct radiative forcing, Journal of
764 Geophysical Research-Atmospheres, 107, 10.1029/2001jd000973, 2002.
765 Li, W. J., and Shao, L. Y.: Observation of nitrate coatings on atmospheric mineral dust
766 particles, Atmos. Chem. Phys., 9, 1863-1871, 10.5194/acp-9-1863-2009, 2009.
767 Lin, Y.-L., Farley, R. D., and Orville, H. D.: Bulk Parameterization of the Snow Field in a
768 Cloud Model, Journal of Climate and Applied Meteorology, 22, 1065-1092, 1983.
769 Liu, Y., Daum, P. H., and McGraw, R. L.: Size truncation effect, threshold behavior, and a
770 new type of autoconversion parameterization, Geophysical Research Letters, 32,
771 L11811, 10.1029/2005gl022636, 2005.
772 Lohmann, U., and Feichter, J.: Global indirect aerosol effects: a review, Atmos. Chem.
773 Phys., 5, 715-737, 10.5194/acp-5-715-2005, 2005.
774 McMichael, A. J., Woodruff, R. E., and Hales, S.: Climate change and human health:
775 present and future risks, The Lancet, 367, 859-869, 2006.
776 Ming, Y., and Russell, L. M.: Organic aerosol effects on fog droplet spectra, Journal of
777 Geophysical Research: Atmospheres, 109, D10206, 10.1029/2003jd004427, 2004.
778 Moore, K. F., Sherman, D. E., Reilly, J. E., and Collett, J. L.: Drop size-dependent chemical
779 composition in clouds and fogs. Part I. Observations, Atmospheric Environment, 38,
780 1389-1402, http://dx.doi.org/10.1016/j.atmosenv.2003.12.013, 2004.
781 Motoi, K.: Electron-microscope study of snow crystal nuclei, Journal of Meterology, 8,
782 151-156, 1951.

783 Niu, S. J., Liu, D. Y., Zhao, L. J., Lu, C. S., Lü, J. J., and Yang, J.: Summary of a 4-Year Fog Field
784 Study in Northern Nanjing, Part 2: Fog Microphysics, Pure and Applied Geophysics, 169,
785 1137-1155, 10.1007/s00024-011-0344-9, 2012.
786 Ramanathan, V., Crutzen, P. J., Kiehl, J. T., and Rosenfeld, D.: Atmosphere - Aerosols,
787 climate, and the hydrological cycle, Science, 294, 2119-2124, 10.1126/science.1064034,
788 2001.
789 Rogers, R. R., and Yau, M. K.: A Short Course in Cloud Physics, Third ed., Butterworth
790 Heinemann, 1989.
791 Schell, B., Ackermann, I. J., Hass, H., Binkowski, F. S., and Ebel, A.: Modeling the formation
792 of secondary organic aerosol within a comprehensive air quality model system, Journal
793 of Geophysical Research: Atmospheres (1984–2012), 106, 28275-28293, 2001.
794 Skamarock, W. C., Klemp, J. B., Dudhia, J., Gill, D. O., Barker, D. M., Duda, M. G., Huang, X.-
795 Y., Wang, W., and Powers, J. G.: A Description of the Advanced Research WRF Version 3,
796 NCAR Technical Note, NCAR/TN-475+STR, 2008.
797 Stelson, A. W.: Urban aerosol refractive index prediction by partial molar refraction
798 approach, Environmental Science & Technology, 24, 1676-1679, 10.1021/es00081a008,
799 1990.
800 Sullivan, R. C., Petters, M. D., DeMott, P. J., Kreidenweis, S. M., Wex, H., Niedermeier, D.,
801 Hartmann, S., Clauss, T., Stratmann, F., Reitz, P., Schneider, J., and Sierau, B.: Irreversible
802 loss of ice nucleation active sites in mineral dust particles caused by sulphuric acid
803 condensation, Atmospheric Chemistry and Physics, 10, 11471-11487, 10.5194/acp-10-
804 11471-2010, 2010.
805 Tegen, I., Lacis, A. A., and Fung, I.: The influence on climate forcing of mineral aerosols
806 from disturbed soils, Nature, 380, 419-422, 10.1038/380419a0, 1996.
807 Tewari, M., Chen, F., Kusaka, H., and Miao, S.: Coupled WRF/Unified Noah/urban-canopy
808 modeling system, NCAR WRF Documentation, NCAR, Boulder, 1-22, 2007.
809 Twomey, S.: POLLUTION AND PLANETARY ALBEDO, Atmospheric Environment, 8,
810 1251-1256, 10.1016/0004-6981(74)90004-3, 1974.
811 Yang, F.: Radiative forcing and climate impact of the Mount Pinatubo volcanic eruption. ,
812 PhD, University of Illinois at Urbana-Champaign., 2000.
813 Yang, M., Howell, S. G., Zhuang, J., and Huebert, B. J.: Attribution of aerosol light
814 absorption to black carbon, brown carbon, and dust in China – interpretations of
815 atmospheric measurements during EAST-AIRE, Atmos. Chem. Phys., 9, 2035-2050,
816 10.5194/acp-9-2035-2009, 2009.
817 Ying, Q., and Kleeman, M. J.: Effects of aerosol UV extinction on the formation of ozone
818 and secondary particulate matter, Atmospheric Environment, 37, 5047-5068, 2003.
819 Ying, Q., Lu, J., Allen, P., Livingstone, P., Kaduwela, A., and Kleeman, M.: Modeling air
820 quality during the California Regional PM10/PM2.5 Air Quality Study (CRPAQS) using
821 the UCD/CIT source-oriented air quality model - Part I. Base case model results,
822 Atmospheric Environment, 42, 8954-8966, DOI 10.1016/j.atmosenv.2008.05.064, 2008.
823 Zaveri, R. A., Easter, R. C., Fast, J. D., and Peters, L. K.: Model for Simulating Aerosol
824 Interactions and Chemistry (MOSAIC), Journal of Geophysical Research: Atmospheres,
825 113, D13204, 10.1029/2007jd008782, 2008.
826 Zaveri, R. A., Barnard, J. C., Easter, R. C., Riemer, N., and West, M.: Particle-resolved
827 simulation of aerosol size, composition, mixing state, and the associated optical and
828 cloud condensation nuclei activation properties in an evolving urban plume, Journal of
829 Geophysical Research: Atmospheres, 115, D17210, 10.1029/2009jd013616, 2010.
830 Zhang, H., DeNero, S. P., Joe, D. K., Lee, H. H., Chen, S. H., Michalakes, J., and Kleeman, M.
831 J.: Development of a source oriented version of the WRF/Chem model and its

832 application to the California regional PM10 / PM2.5 air quality study, Atmos. Chem.
833 Phys., 14, 485-503, 10.5194/acp-14-485-2014, 2014.
834

835

836

837 **Captions of Tables**

838 Table 1. Chemical species that are carried in the AQC/CLDAQC "species" dimension. All
839 species are in concentrations (μg m^{-3}) except for the last two elements (i.e., 39 and
840 40), which carry the number concentration (# m^{-3}) and radius (m).

841 Table 2. California Ambient Air Quality Data (CAAQD) station information.

842 Table 3. Numerical experiment designs for this study.

843 Table 4. Hourly bias mean and standard deviation (std) in day time and night time of 2-m
844 temperature (T2, °C), water vapor mixing ratio (Q2, g kg-air^{-1}), and net downward
845 shortwave radiative flux (NSF, W m^{-2}) between all experiments and observation from
846 16 to 18 January 2011. T2 and Q2 are calculated using 24 surface stations and NSF is
847 calculated using 42 CIMIS stations shown in Fig. 4.

848 Table 5. Mean values of cloud water mixing ratio (Q_c), cloud droplet number (Q_n), surface
849 skin temperature (SKT), net shortwave flux (NSF), latent heat flux (LH) and sensible
850 heat flux (SH) for four experiments over the entire Central Valley during 16 to 18
851 January 2011.

852 Table 6. Ratio of AQC number concentration for each bin/source averaged within the first
853 five model layers during 16 to 18 January 2011.

854 Table 7. Hourly bias mean and root-mean-square-difference of cloud water mixing ratio (Q_c),
855 cloud droplet number (Q_n), surface skin temperature (SKT), net shortwave flux
856 (NSF), latent heat flux (LH) and sensible heat flux (SH) between internally mixed
857 (I_ARon_CRmod) and source-oriented (S_ARon_CRmod) experiments (internally
858 mixed – source-oriented) during 16 to 18 January 2011.

859
860

861 **Captions of Figures**

862 Figure 1. Cloud physics processes that are involved with cloud particles in the SOWC model
863 with a 6D aerosol variable (AQC) and a 6D cloud variable (CLDAQC) included.
864 Black solid arrow and grey dashed arrow indicate the source and the sink processes of
865 cloud water and 6D CLDAQC, as well as 6D AQC, respectively.

866 Figure 2. MODIS true color image at (a) 1930 UTC 16 January 2011 and (b) 1835 UTC 17
867 January 2011 from Satellite Terra, respectively.

868 Figure 3. The column integrated water vapor (shaded; mm), 850-hPa wind vector, and seal
869 level pressure (contours; hPa) from ECMWF Interim reanalysis at (a) 0000 UTC (4
870 pm local time) 11 January, (b) 0000 UTC 12 January, (c) 0000 UTC 13 January, (d)
871 0000 UTC 14 January, (e) 0000 UTC 15 January, (f) 0000 UTC 16 January, (g) 0000
872 UTC 17 January, and (h) 0000 UTC 18 January, 2011.

873 Figure 4. NOAA's National Climatic Data Center (NCDC; 24 stations, red dots), California
874 Irrigation Management Information System (CIMIS; 42 stations, black dots) and
875 California Ambient Air Quality Data (6 stations, numbers corresponding to Table 2
876 station ID) measurement locations. Shaded is terrain height in m.

877 Figure 5. The 72-hour averaged (16 to 18 January 2011) AQC number concentration
878 averaged over the first five model layers from the polluted experiment
879 (S_ARon_CRmod) in units of 10^8 # m^{-3}. Contours are terrain heights in m.

880 Figure 6. Comparison of (a) Nitrate (NO_3^-), (b) Sulfate (SO_4^{2-}), (c) Ammonium (NH_4^+), and
881 (d) Soluble Sodium (Na^+) between simulated source-oriented experiment
882 (S_ARon_CRmod), internally mixed experiment (I_ARon_CRmod) and the observed
883 concentrations of airborne particles on 18 January 2011. Units are μg m^{-3}.

884 Figure 7. Liquid water path (LWP) (g m^{-2}) from MODIS Level 2 cloud products ((a), (c) and

885 (e)) and from the SOWC model with aerosol feedback on and modified cloud-
886 radiation scheme (S_ARon_CRmod; (b), (d) and (e)). (a) and (b) are at 1900 UTC 16
887 January 2011. (c) and (d) are at 1800 UTC 17 January 2011. (e) and (f) are at 1900
888 UTC 18 January 2011. Contours in (b), (d) and (e) are terrain heights in m.
889 Figure 8. Same as Figure 5 but cloud optical thickness (COT) (dimensionless).
890 Figure 9. Mean bias variation of (a) 2-m temperature (T2), (b) 2-m water vapor mixing ratio
891 (Q2), and (c) surface net downward shortwave radiative flux (NSF) between
892 observations and model simulation from 16 to 18 January 2011 for S_ARon_CRmod
893 (blue lines), S_ARoff_CRmod (purple lines) and I_ARon_CRmod (red lines)
894 experiments.
895 Figure 10. N_{CCN}/N_{CN} ratio for (a) S_ARon_CRmod (source-oriented experiment) and (b)
896 I_ARon_CRmod (internally mixed experiment) averaged within the first five model
897 layers. The ratio is hourly average during 16 to 18 January 2011. Contours are
898 terrain heights in m.
899 Figure 11. (a) 72-hour averaged CCN concentration at supersaturation of 0.02%, 0.05%,
900 0.1%, 0.2%, 0.5% and total AQC concentration with units in # cm^{-3}. (b) N_{CCN}/N_{CN}
901 ratio at 5 corresponding supersaturation. Dark gray is source-oriented experiment and
902 light gray represents internally mixed experiment. Results are average values using
903 data within the first five model layers.
904 Figure 12. Relative change ((internally mixed – source-oriented)/source-oriented * 100%) in
905 72-hour averaged predictions during 16 to 18 January 2011 for (a) the ratio of cloud
906 water mixing ratio, (b) cloud droplet number, (c) surface skin temperature and (d) net
907 shortwave radiation. (a) and (b) are average values using data within the first five
908 model layers. Contours are terrain heights in m.
909 Figure 13. Area average of latent heat flux (LH) and sensible heat flux (SH) over the Central

910 Valley in S_ARon_CRmod and the average difference between I_ARon_CRmod and
911 S_ARon_CRmod from 0800 UTC 17 January (00 Z local time) to 0700 UTC 18 January
912 (23 Z local time).

913

914

915 Table 1. Chemical species that are carried in the AQC/CLDAQC "species" dimension. All
916 species are in concentrations (μg m^{-3}) except for the last two elements (i.e., 39 and 40), which
917 carry the number concentration (# m^{-3}) and radius (m).

	Chemical species		Chemical species
1	EC	21	SOA from lumped Alkane 1
2	OC	22	SOA from lumped Alkane 2
3	NA	23	SOA from lumped Aromatic 1
4	CL	24	SOA from lumped Aromatic 2
5	N3	25	SOA from lumped Aromatic 1
6	S6	26	SOA from lumped Aromatic 2
7	N5	27	SOA from lumped Aromatic 1
8	Other	28	SOA from lumped Aromatic 2
9	Metal	29	SOA from lumped Alkene 1
10	Unknown	30	SOA from lumped Alkene 2
11	CU1	31	SOA from lumped Alpha Pinene 1
12	CU2	32	SOA from lumped Alpha Pinene 2
13	MN2	33	SOA from lumped Beta Pinene 1
14	MN3	34	SOA from lumped Beta Pinene 2
15	FE2	35	SOA from lumped Toluene 1
16	FE3	36	SOA from lumped Toluene 2
17	S4	37	Hydrogen Ion
18	Air (hollow sea salt particles)	38	Water
19	NO3	39	Number Concentration
20	Non-explicit SOA	40	Particle Mean Volume Radius

918

919

920

921

Table 2. California Ambient Air Quality Data (CAAQD) station information

Station ID	Station name	Longitude (º)	Latitude (º)
1	San Jose-Jackson Street	-121.89	37.35
2	Bakersfield-5558 Cal. Avenue	-119.06	35.36
3	Fresno-1st Street	-119.77	36.78
4	Modesto-14th Street	-120.99	37.64
5	Visalia-N Church Street	-119.29	36.33
6	Sacramento-T Street	-121.49	38.57

928 Table 3. Numerical experiment designs for this study.

Experiments	Description
S_ARon_CRmod	Source-Oriented aerosols with aerosol direct effect calculation on and modified cloud radiation parameterization
S_ARon_CRorig	Source-Oriented aerosols with aerosol direct effect calculation on and original cloud radiation parameterization
S_AROff_CRmod	Source-Oriented aerosols with aerosol direct effect calculation off and modified cloud radiation parameterization
I_ARon_CRmod	Internal mixing aerosols with aerosol direct effect calculation on and modified cloud radiation parameterization

929

Table 4. Hourly bias mean and standard deviation (std) in day time and night time of 2-m temperature (T2, °C), water vapor mixing ratio (Q2, g kg-air^{-1}), and net downward shortwave radiative flux (NSF, W m^{-2}) between all experiments and observation from 16 to 18 January 2011. T2 and Q2 are calculated using 24 surface stations and NSF is calculated using 42 CIMIS stations shown in Fig. 4.

	S_ARon_CRmod		S_ARon_CRorig		S_ARoff_CRmod		I_ARon_CRmod	
Daytime	Bias mean	std	Bias mean	std	Bias mean	std	Bias mean	std
T2	-1.76	1.27	-1.72	1.32	-1.63	1.33	-2.01	1.09
Q2	-0.56	0.34	-0.56	0.36	-0.54	0.35	-0.57	0.32
NSF	13.91	53.18	14.40	58.00	18.81	58.78	8.68	50.03
Nighttime	Bias mean	std	Bias mean	std	Bias mean	std	Bias mean	std
T2	-2.22	0.92	-2.21	0.95	-2.19	0.93	-2.30	0.87
Q2	-0.88	0.41	-0.87	0.42	-0.88	0.42	-0.89	0.41
NSF	/	/	/	/	/	/	/	/

Table 5. Mean values of cloud water mixing ratio (Q_c), cloud droplet number (Q_n), surface skin temperature (SKT), net shortwave flux (NSF), latent heat flux (LH) and sensible heat flux (SH) for four experiments over the entire Central Valley during 16 to 18 January 2011.

	S_ARon_CRmod	S_ARon_CRorig	S_AROff_CRmod	I_ARon_CRmod
Q_c^* (g m^{-3})	0.220	0.221	0.213	0.231
Q_n^* (# m^{-3})	3.94×10^8	4.18×10^8	3.77×10^8	4.57×10^8
SKT (K)	281.305	281.30	281.404	281.151
NSF** (W m^{-2})	130.56	131.02	134.24	124.54
LH (W m^{-2})	9.01	9.02	9.36	8.40
SH (W m^{-2})	4.91	4.55	5.27	4.54
COT (unitless)	25.56	25.15	24.49	28.62

* Averaged within the first five model layers

** Averaged only in the daytime

Table 6. Ratio of AQC number concentration for each bin/source averaged within the first five model layers during 16 to 18 January 2011.

	Wood smoke	Gasoline	Diesel	Meat cooking	Others	Source-oriented	Internal
Bin1	28.92%	1.00%	4.25%	0.84%	10.39%	45.40%	48.89%
Bin2	9.12%	0.38%	1.48%	0.60%	38.64%	50.22%	46.74%
Bin3	0.19%	0.01%	0.03%	0.02%	3.03%	3.28%	3.26%
Bin4	0.00%	0.00%	0.00%	0.00%	0.17%	0.18%	0.21%
Bin5	0.00%	0.00%	0.00%	0.00%	0.02%	0.02%	0.02%
Bin6	0.00%	0.00%	0.00%	0.00%	0.00%	0.00%	0.00%
Bin7	0.00%	0.00%	0.00%	0.00%	0.00%	0.00%	0.00%
Bin8	0.00%	0.00%	0.00%	0.00%	0.91%	0.91%	0.88%

948 Table 7. Hourly bias mean and root-mean-square-difference of cloud water mixing ratio (Q_c),
949 cloud droplet number (Q_n), surface skin temperature (SKT), net shortwave flux (NSF), latent
950 heat flux (LH) and sensible heat flux (SH) between internally mixed (I_ARon_CRmod) and
951 source-oriented (S_ARon_CRmod) experiments (internally mixed – source-oriented) during
952 16 to 18 January 2011.

	Bias mean	**Root-mean-square-difference**
Q_c^* (g m^{-3})	1.19×10^{-2}	4.16×10^{-2}
Q_n^* (# m^{-3})	6.24×10^{7}	2.64×10^{8}
SKT (K)	-0.15	0.57
NSF (W m^{-2})	-6.02	13.30
LH (W m^{-2})	-0.61	2.75
SH (W m^{-2})	-0.36	5.24

953 * Averaged within the first five model layers

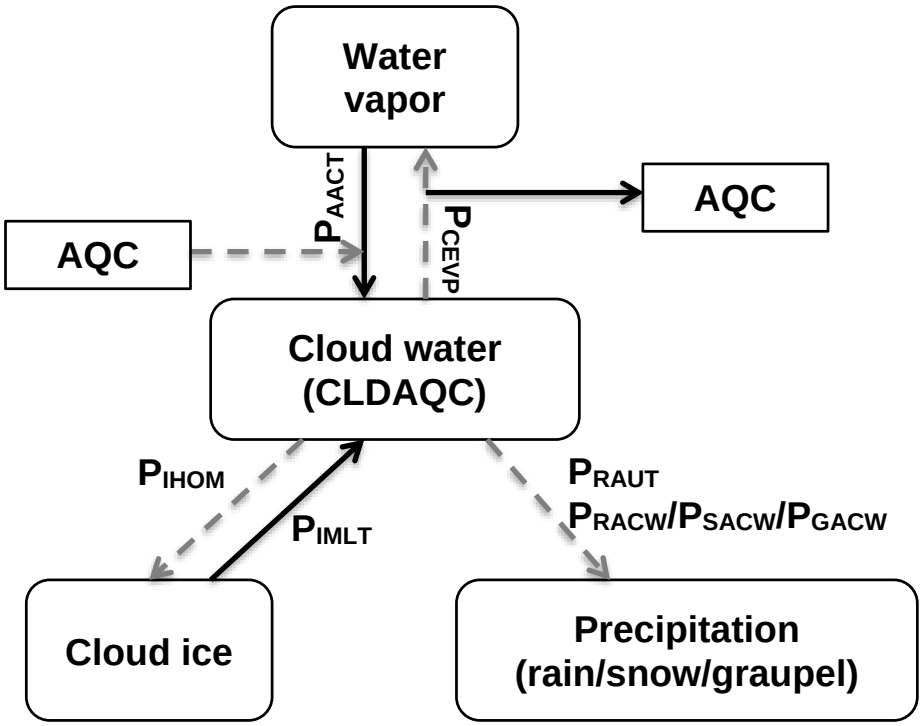

Figure 1. Cloud physics processes that are involved with cloud particles in the SOWC model with a 6D aerosol variable (AQC) and a 6D cloud variable (CLDAQC) included. Black solid arrow and grey dashed arrow indicate the source and the sink processes of cloud water and 6D CLDAQC, as well as 6D AQC, respectively.

(a)

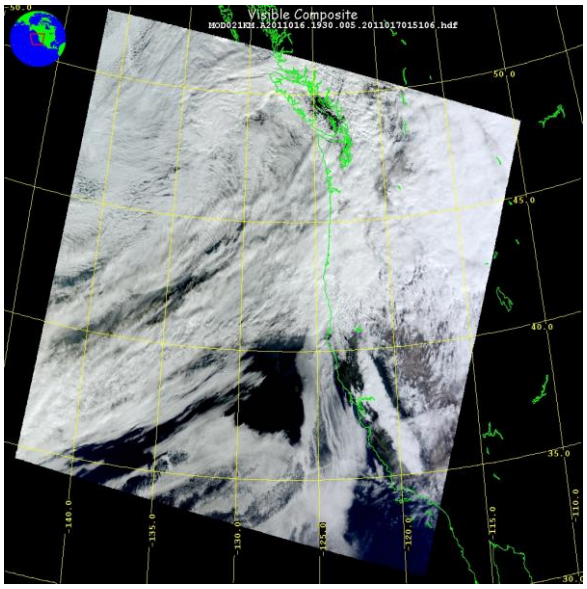

(b)

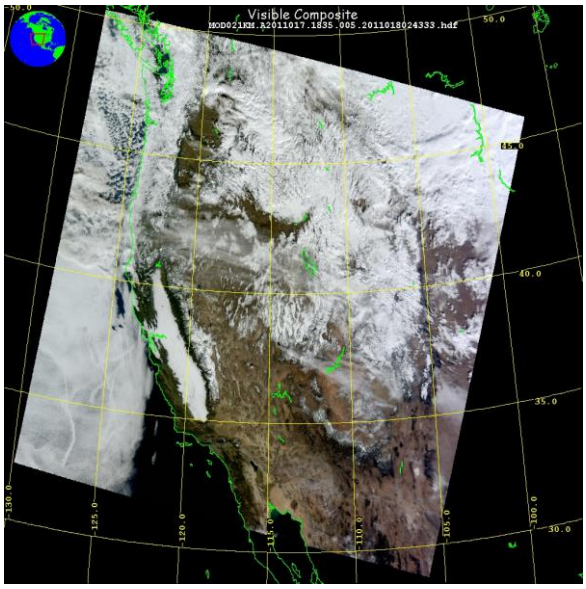

(c)

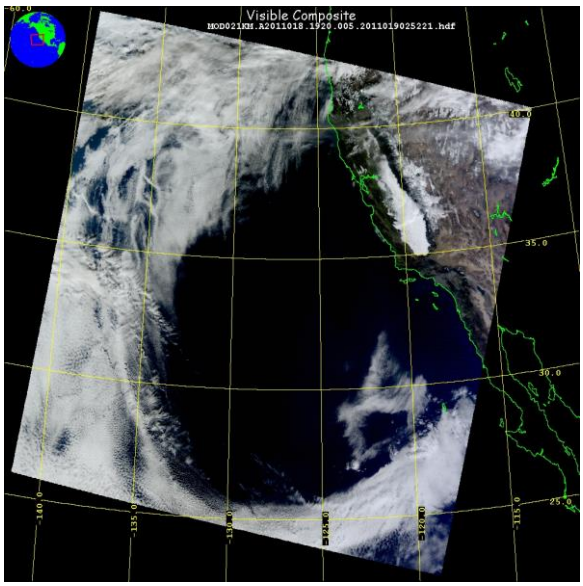

Figure 2. MODIS true color images at (a) 1930 UTC 16 January, (b) 1835 UTC 17 January, and (c) 1920 UTC 18 January, 2011 from Satellite Terra.

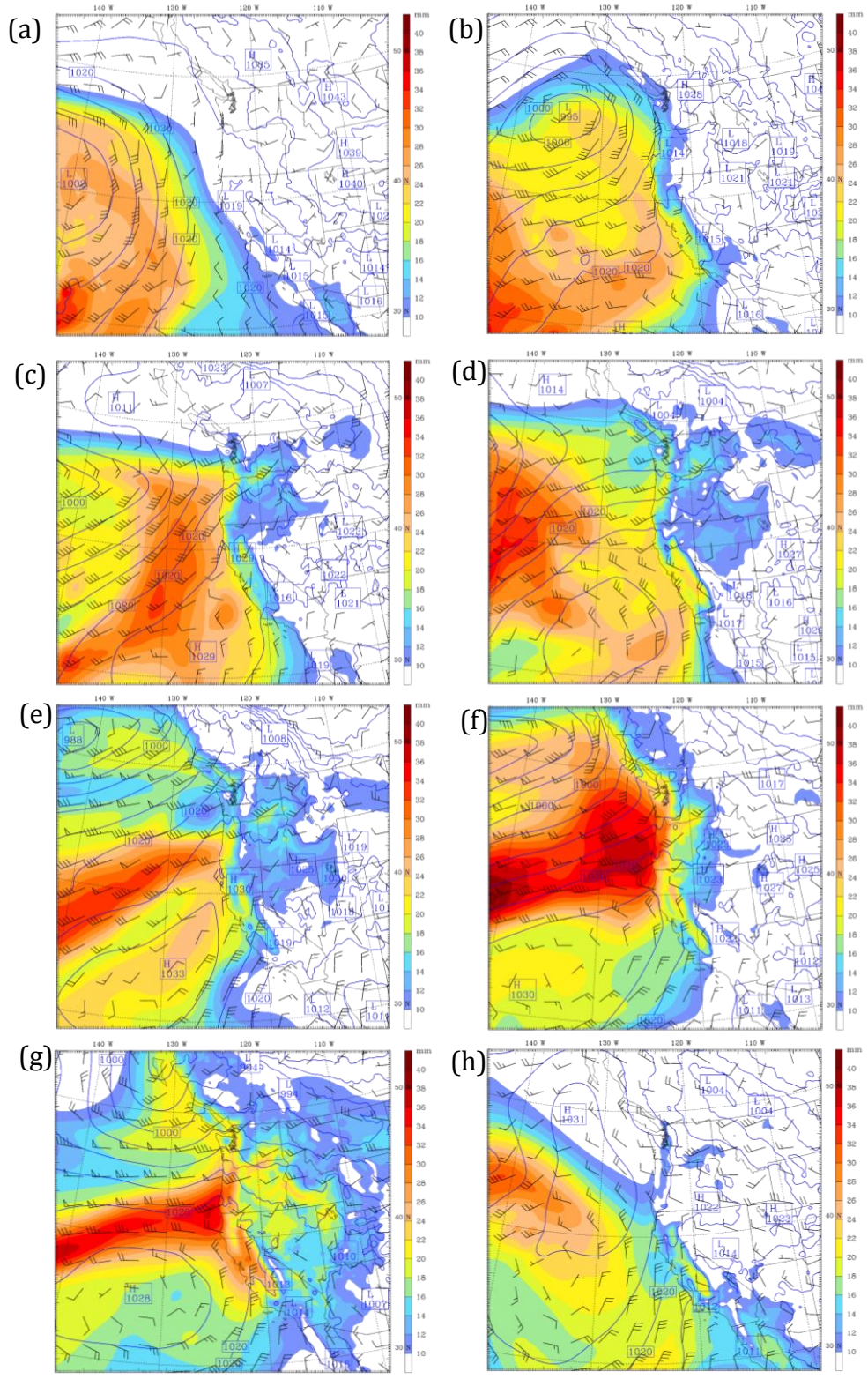

Figure 3. The column integrated water vapor (shaded; mm), 850-hPa wind vector, and sea level pressure (contours; hPa) from ECMWF Interim reanalysis at (a) 0000 UTC (4 pm local time) 11 January, (b) 0000 UTC 12 January, (c) 0000 UTC 13 January, (d) 0000 UTC 14 January, (e) 0000 UTC 15 January, (f) 0000 UTC 16 January, (g) 0000 UTC 17 January, and (h) 0000 UTC 18 January, 2011.

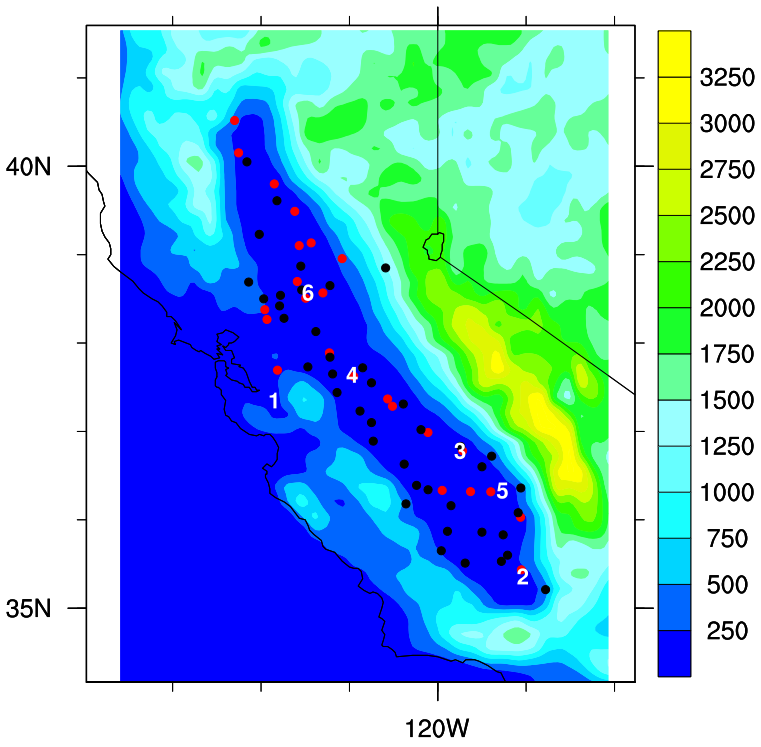

Figure 4. NOAA's National Climatic Data Center (NCDC; 24 stations, red dots), California Irrigation Management Information System (CIMIS; 42 stations, black dots) and California Ambient Air Quality Data (6 stations, numbers corresponding to Table 2 station ID) measurement locations. Shaded is terrain height in m.

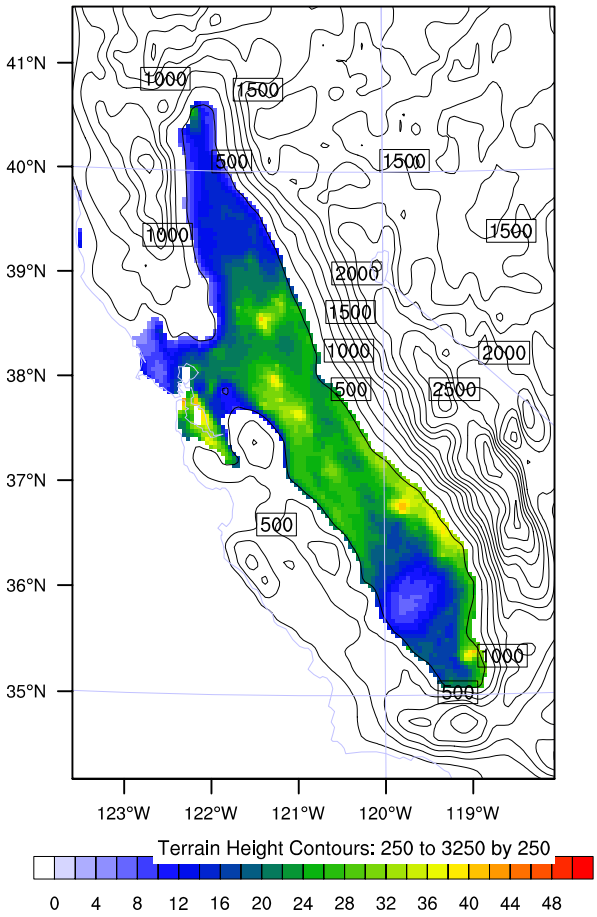

Figure 5. The 72-hour averaged (16 to 18 January 2011) AQC number concentration averaged over the first five model layers from the experiment S_ARon_CRmod in units of 10^8 # m^{-3}. Contours are terrain heights in m.

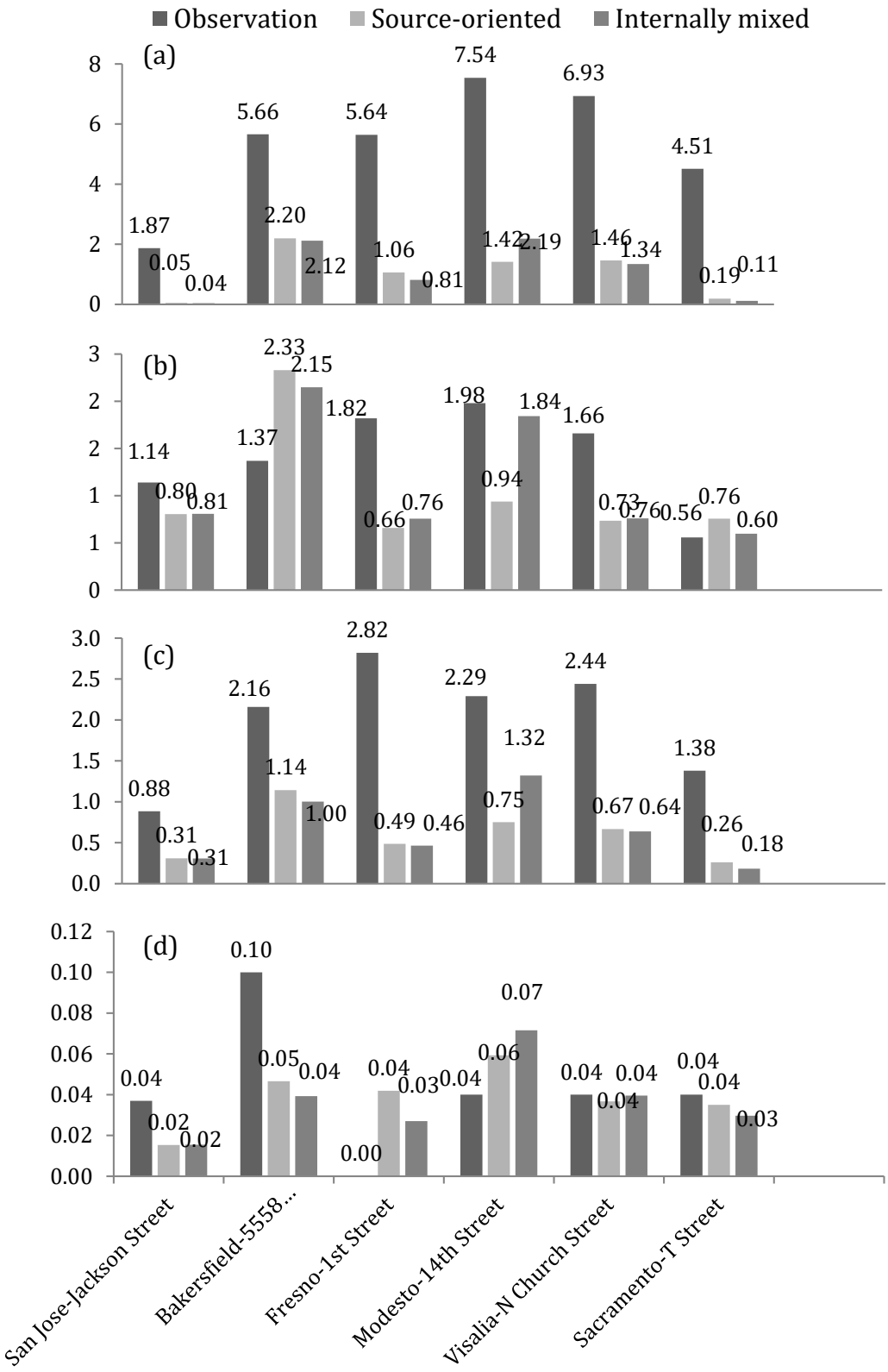

Figure 6. Comparison of (a) Nitrate (NO_3^-), (b) Sulfate (SO_4^{2-}), (c) Ammonium (NH_4^+), and (d) Soluble Sodium (Na^+) between simulated source-oriented experiment (S_ARon_CRmod), internally mixed experiment (I_ARon_CRmod) and the observed concentrations of airborne particles on 18 January 2011. Units are μg m^{-3}.

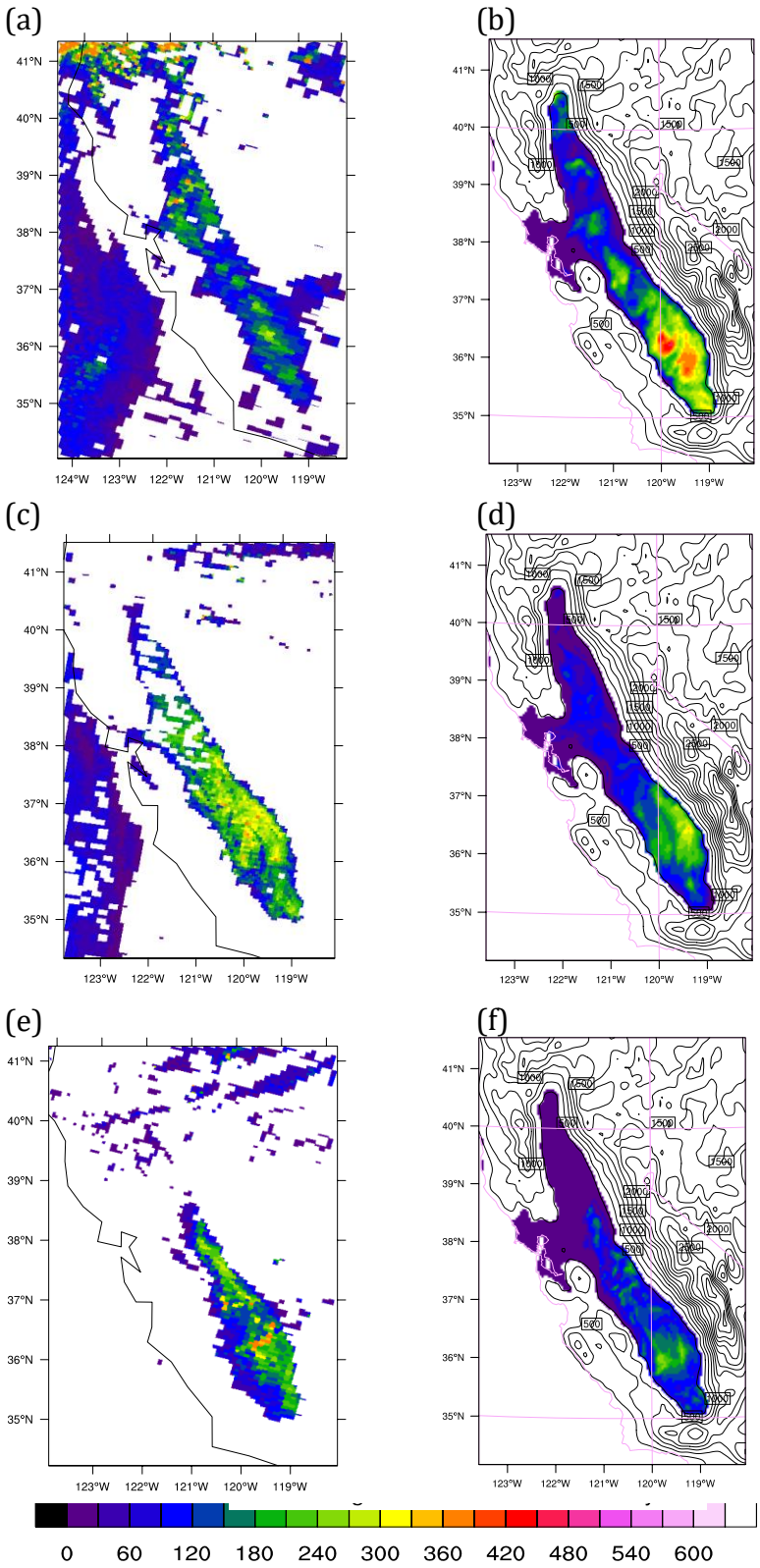

Figure 7. Liquid water path (LWP) (g m^{-2}) from MODIS Level 2 cloud products ((a), (c) and (e)) and from the SOWC model with aerosol feedback on and modified cloud-radiation scheme (S_ARon_CRmod; (b), (d) and (e)). (a) and (b) are at 1900 UTC 16 January 2011. (c) and (d) are at 1800 UTC 17 January 2011. (e) and (f) are at 1900 UTC 18 January 2011. Contours in (b), (d) and (e) are terrain heights in m.

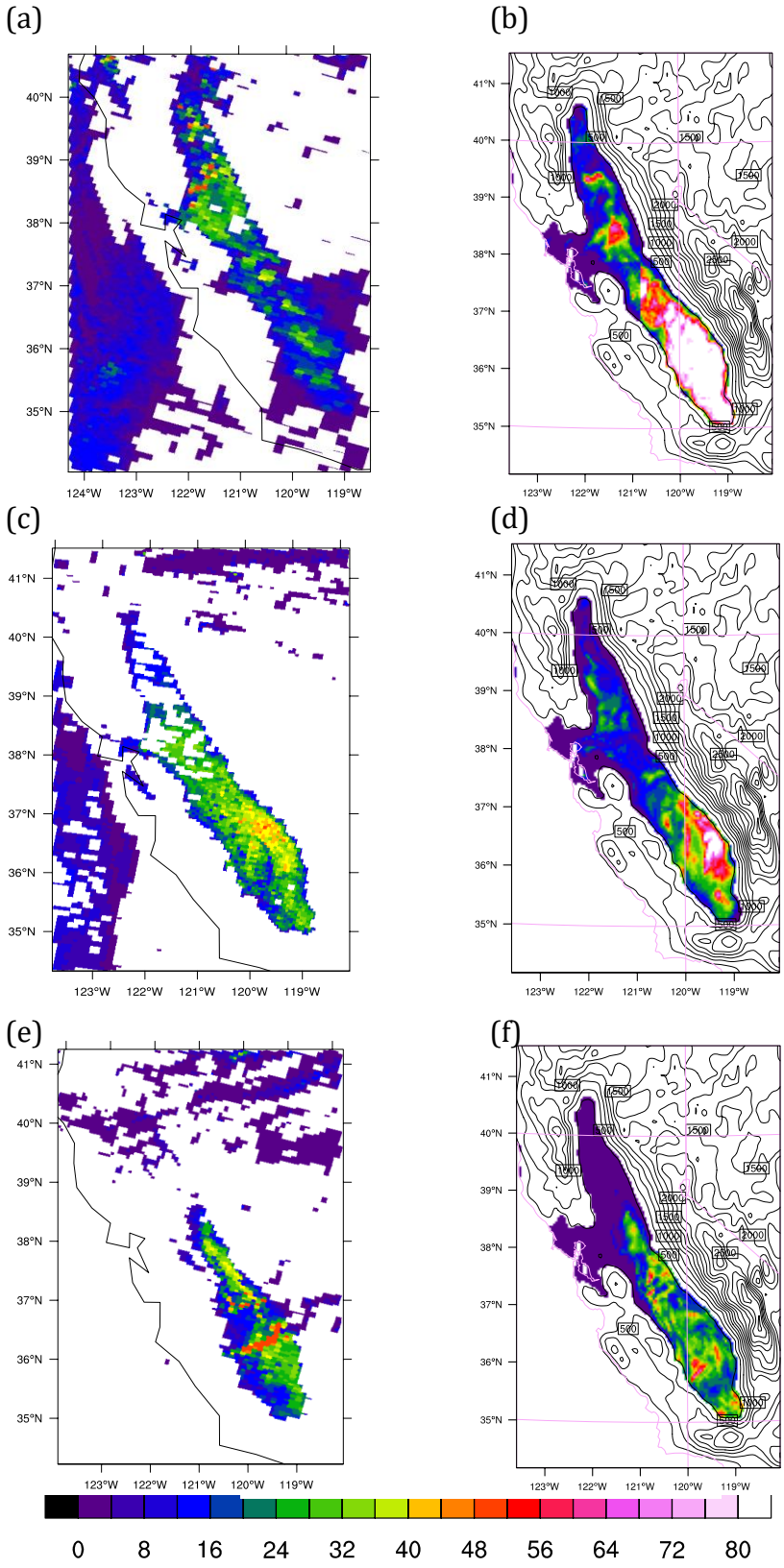

Figure 8. Same as Figure 5 but cloud optical thickness (COT) (dimensionless).

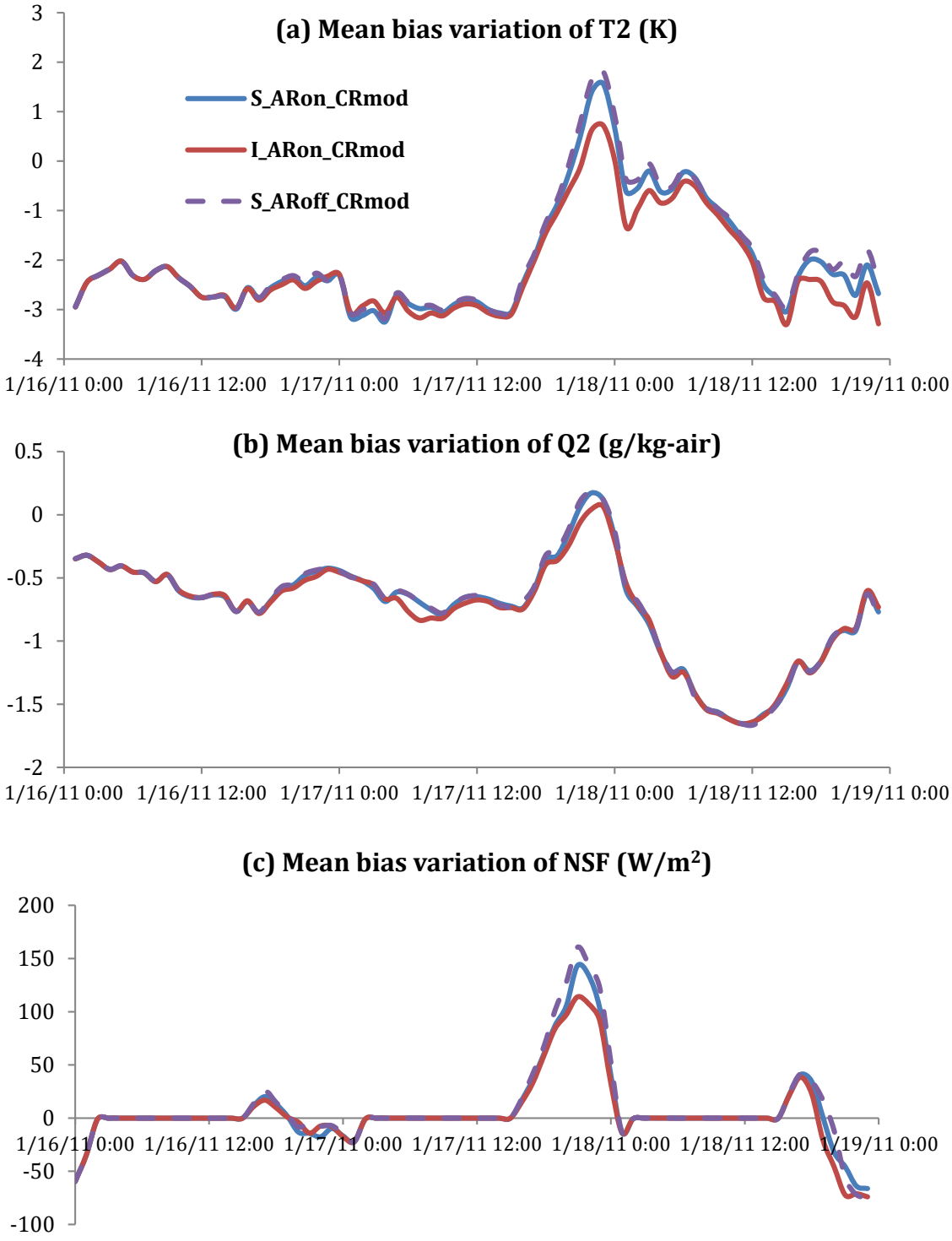

Figure 9. Mean bias variation of (a) 2-m temperature (T2), (b) 2-m water vapor mixing ratio (Q2), and (c) surface net downward shortwave radiative flux (NSF) between observations and model simulation from 16 to 18 January 2011 for S_ARon_CRmod (blue lines), S_ARoff_CRmod (purple lines) and I_ARon_CRmod (red lines) experiments.

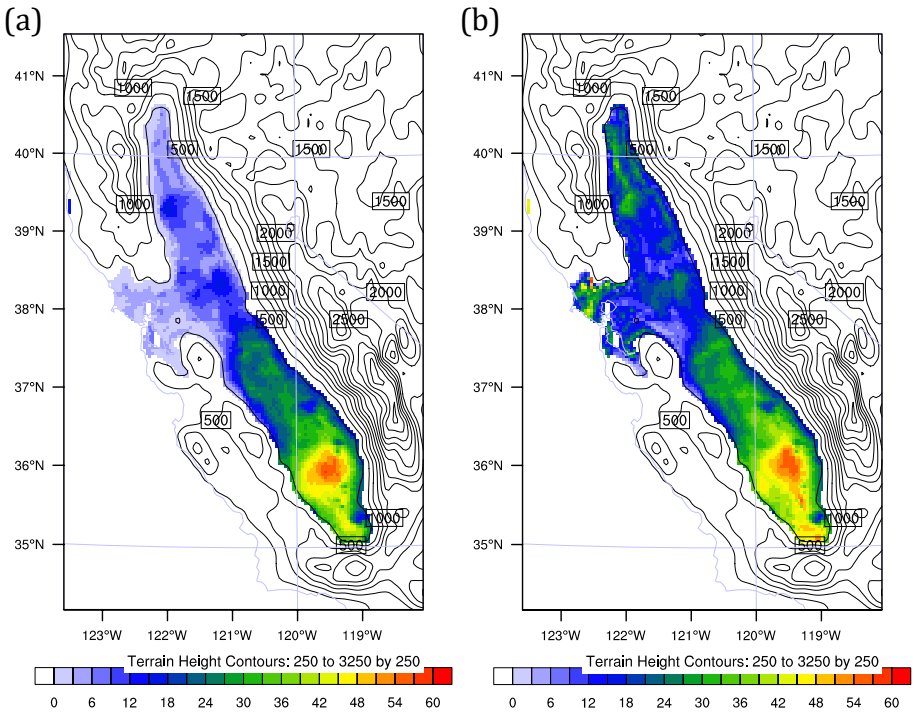

Figure 10. N_{CCN}/N_{CN} ratio for (a) S_ARon_CRmod (source-oriented experiment) and (b) I_ARon_CRmod (internally mixed experiment) averaged within the first five model layers. The ratio is hourly average during 16 to 18 January 2011. Contours are terrain heights in m.

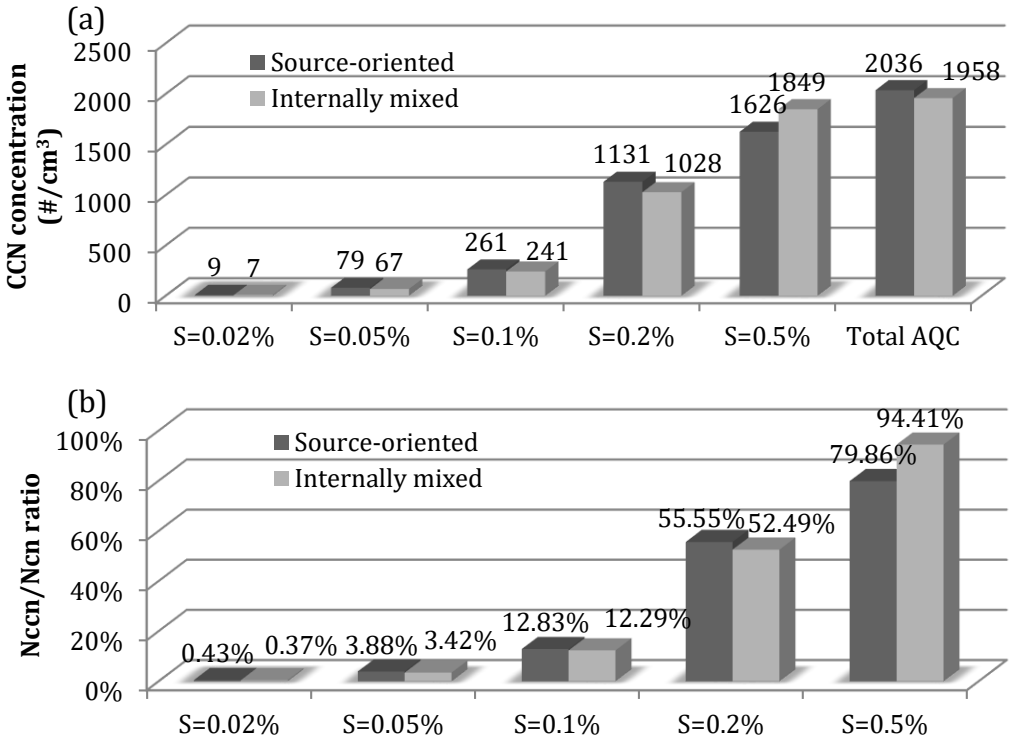

Figure 11. (a) 72-hour averaged CCN concentration at supersaturation of 0.02%, 0.05%, 0.1%, 0.2%, 0.5% and total AQC concentration with units in # cm^{-3}. (b) N_{CCN}/N_{CN} ratio at 5 corresponding supersaturation. Dark gray is source-oriented experiment and light gray represents internally mixed experiment. Results are average values using data within the first five model layers.

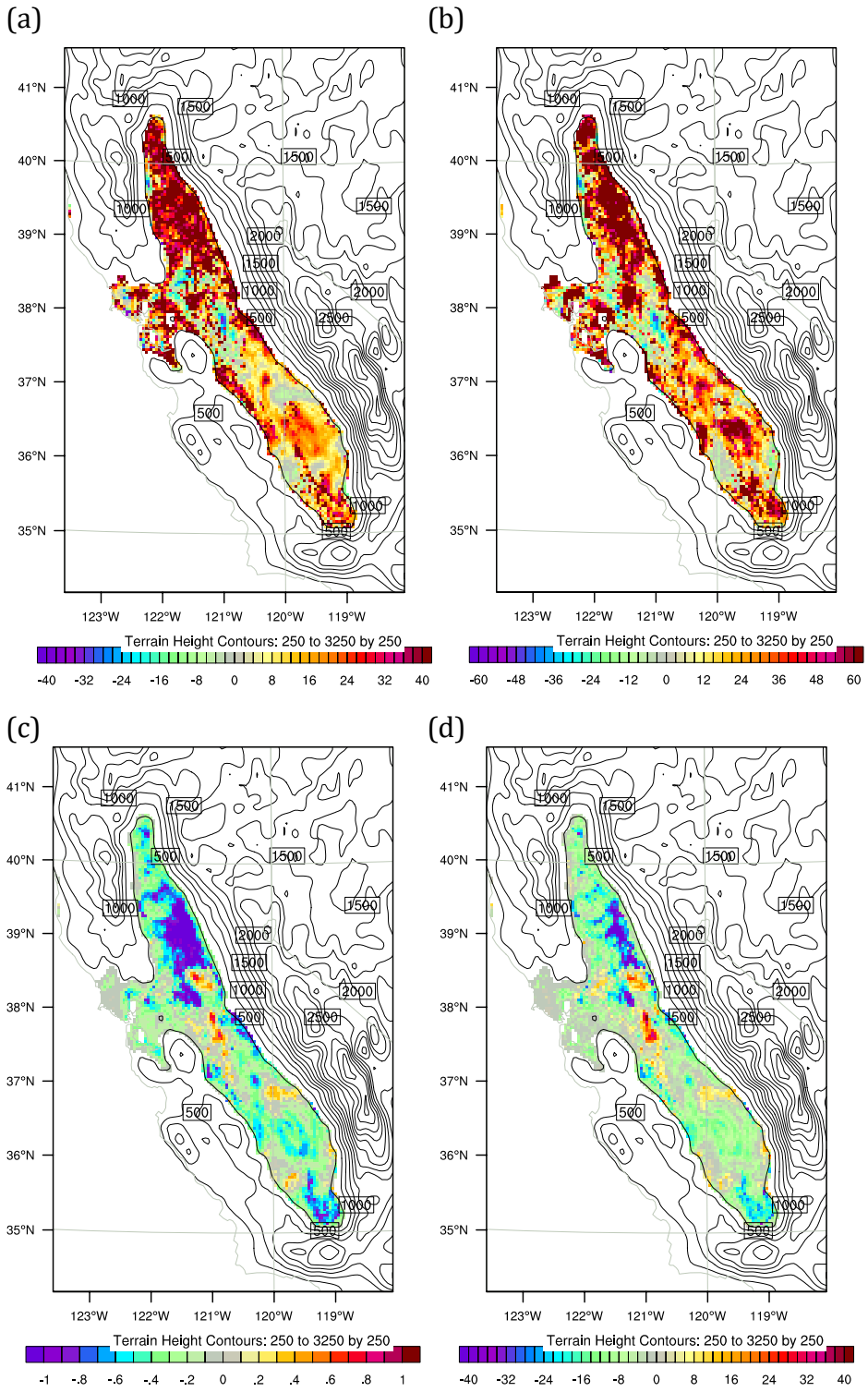

Figure 12. Relative change ((internally mixed – source-oriented)/source-oriented * 100%) in the daytime averaged predictions during 16 to 18 January 2011 for (a) the ratio of cloud water mixing ratio, (b) cloud droplet number and absolute difference (internally mixed – source-oriented) in (c) surface skin temperature (K) and (d) net shortwave radiation (W m^{-2}). (a) and (b) are average values using data within the first five model layers. Contours are terrain heights in m.

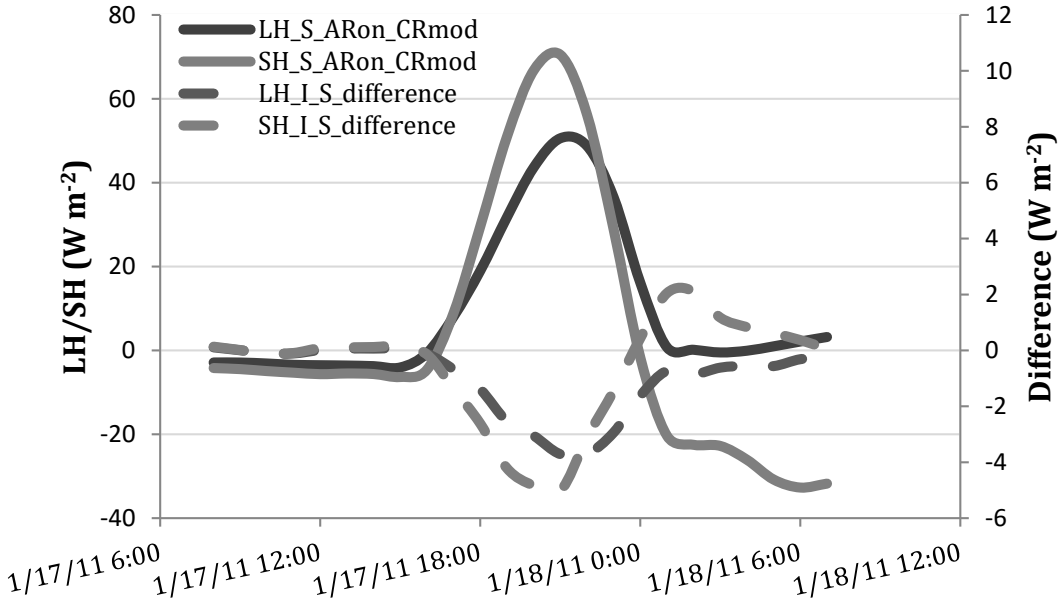

Figure 13. Area average of latent heat flux (LH) and sensible heat flux (SH) over the Central Valley in S_ARon_CRmod and the average difference between I_ARon_CRmod and S_ARon_CRmod from 0800 UTC 17 January (00 Z local time) to 0700 UTC 18 January (23 Z local time).